



A Non-Reciprocal Channel Model for THz Asymmetric Massive MIMO Systems

Journal:	<i>IEEE Transactions on Wireless Communications</i>
Manuscript ID	Paper-TW-Mar-23-0388.R1
Manuscript Type:	Original Transactions Paper
Date Submitted by the Author:	17-Aug-2023
Complete List of Authors:	Zhang, Kaien; Beijing Institute of Technology, School of Information and Electronics Zhang, Yan; Beijing Institute of Technology, School of Information and Electronics Wang, Cheng-Xiang; Southeast University, National Mobile Communications Research Laboratory; Purple Mountain Laboratories, Pervasive Communication Research Center Wu, Xiping; University College Dublin, School of Electrical and Electronic Engineering Du, Chuan; Beijing Institute of Technology, School of Information and Electronics
Keyword:	

A Non-Reciprocal Channel Model for THz Asymmetric Massive MIMO Systems

Kaien Zhang, Yan Zhang, Cheng-Xiang Wang, *Fellow, IEEE*,
Xiping Wu, *Senior Member, IEEE*, and Chuan Du

Abstract—Non-reciprocal antenna beam patterns are promising to be utilized in asymmetric massive multiple-input multiple-output (MIMO) systems for future sixth-generation communications. The inconsistency of uplink (UL) and downlink (DL) channels makes channel modeling in this scenario challenging. In this paper, a novel geometry-based stochastic model (GBSM) is proposed for non-reciprocal terahertz (THz) channels. A directional effective scatterer generation algorithm is designed to depict the inconsistency of bidirectional propagation conditions. The correlation function between UL and DL is derived and analyzed, which validates the ability to characterize the non-reciprocal channels. To mimic THz propagation features, molecular absorption and diffuse scattering are introduced to the model, which is verified by measured data. In addition, the non-stationarities in space, time, and frequency domains are characterized, respectively. Statistical properties are compared between analytical and simulation results, and good agreements are shown. Finally, the accuracy of the model is verified by comparing with the ray tracing data.

Index Terms—Asymmetric massive multiple-input multiple-output (MIMO) system, geometry-based stochastic model (GBSM), non-reciprocal beam patterns, space-time-frequency non-stationarity, terahertz (THz) channel modeling.

I. INTRODUCTION

IN the aim of satisfying the ever-growing demand for high data rates in wireless communication systems, the support of massive data traffic in urban scenarios, where users are highly intensified, is required [1], [2]. The forthcoming beyond fifth-generation (B5G) and sixth-generation (6G) wireless communication systems are expected to support gigabits or even several terabits per second with low latency and cost [3]–[5], which are operated over a wide spectrum. For hot-spot high-capacity scenarios, the urgent challenges to be solved are high data transmission rates and extremely high traffic

This work was supported by the National Key Research and Development Program of China (No. 2020YFB1804901), the Defense Industrial Technology Development Program, China under Grant JCKY2022209A001, the National Natural Science Foundation of China (No. 62271051 and No. 61960206006), and the Key Technologies Research and Development Program of Jiangsu (Prospective and Key Technologies for Industry) (No. BE2022067, BE2022067-1). (Corresponding author: Cheng-Xiang Wang and Yan Zhang.)

Kaien Zhang, Yan Zhang, and Chuan Du are with the School of Information and Electronics, Beijing Institute of Technology, Beijing 100081, China (e-mail: 3120210829@bit.edu.cn; zhangy@bit.edu.cn; duchuan95@outlook.com).

Cheng-Xiang Wang is with the National Mobile Communications Research Laboratory, School of Information Science and Engineering, Southeast University, Nanjing, 210096, China, and also with the Purple Mountain Laboratories, Nanjing, 211111, China (email: chxwang@seu.edu.cn).

Xiping Wu is with the School of Electrical and Electronic Engineering, University College Dublin, Dublin 4, D04 V1W8 Ireland (e-mail: xip-ing.wu@ucd.ie).

density, so the spectral efficiency of the system needs to be greatly improved. Massive multiple-input multiple-output (MIMO) technology is one of the most important enabling technologies which can achieve high spectral efficiency, and deploy sector-specific or user-specific beamforming to enhance signal strength and reduce multi-user interference [6]. The massive MIMO system can effectively improve energy efficiency to reduce the transmit power, and because the large-scale antennas average the effect of small-scale fading, it provides superior performance for communication systems.

Conventionally in the communication between the base station (BS) and mobile station (MS), identical beam patterns are adopted for both transmitting and receiving at one side. The uplink (UL) and downlink (DL) share the same beamwidth properties, regardless of the fact that discrepancies may exist in bidirectional propagation environments [7]. Additionally, some drawbacks exist in the antenna arrays with reciprocal beam patterns, such as high computational complexity, hardware cost, and energy consumption, limiting the large-scale deployment and application of high-frequency communication systems [8].

To meet the performance challenges of traditional MIMO arrays, full-digital asymmetric massive MIMO systems using non-reciprocal antenna arrays were designed and validated recently [8]–[10]. Here, the antenna arrays with non-reciprocal transmitting and receiving beam patterns and beamforming are defined as non-reciprocal (beamforming) arrays [10]. For example, on the BS side, a larger-scale array is used for transmitting and a smaller-scale array is used for receiving. As a result, narrower beamwidth is deployed in DL and wider one is deployed in UL for the BS. Compared with traditional arrays with reciprocal beam patterns, the non-reciprocal arrays have advantages in link gain, beam alignment, communication system capacity, and hardware design complexity. In [10], it was proven that the non-reciprocal array configurations could provide wider coverage (more user access) for UL and high-gain beam (better signal-to-noise ratio) for DL. The non-reciprocal arrays can be a potential candidate in future massive MIMO communication systems because of their good energy efficiency and low complexity [9], [10].

Meanwhile, due to different beam patterns deployed for transmitting and receiving arrays, electromagnetic waves experience different propagation processes in the DL and UL channels, which is different from traditional symmetric communication systems. As a consequence, channel responses and characteristics are not identical anymore in the DL and UL, and non-reciprocal channels are formed resulting from asym-

metric beam configurations. The challenges to non-reciprocal channel modeling lie in how to couple the beam domain and the scattering environment, how to establish and utilize the relationship between both directions, and how to simultaneously model the DL and UL channels to reduce complexity. Although effort was paid to the non-reciprocal beamforming design by academia recently [10], channel modeling and characterizing on asymmetric massive MIMO systems are still in the research gap. For the design, simulation, and optimization of the asymmetric massive MIMO systems, it is worthwhile to include non-reciprocity into channel modeling.

Some research works were carried out to model the relationship between the beamwidth and channel properties. According to directional channel measurement campaigns in the literature, the antenna beamwidth has an effect on channel statistical properties such as path loss [11], delay spread [12], [13], and angular spread [12]. Empirical fitting models of corresponding channel parameters and beamwidths were given in these literature. In [14], the beamwidth was considered as an impact factor in statistical channel modeling. The research works mentioned above merely provided empirical models of beamwidth, and may be not suitable for link-level simulations. In [15], a semi-deterministic MIMO-based beam channel model based on ray-tracing and propagation-graph was proposed, but only DL channel responses were given. In [16], joint angular distribution for non-reciprocal beams via the mixture of Gaussian distribution was analyzed. Analysis of asymmetric beam channel characteristics based on geometric model was conducted in [17]. Beam domain channel models for B5G communications were proposed in [18]–[20]. In [21], UL channel parameters were predicted by DL ones using ensemble-transfer learning. In [22], the authors proposed a beam-related path loss prediction method via attention mechanism. In summary, for the asymmetric massive MIMO systems, the bidirectional channel response model is urgently needed.

Furthermore, to support the construction and realization of asymmetric massive MIMO communication systems, the terahertz (THz) band ranging from 100 GHz to 10 THz has become a promising candidate frequency band [23]–[26]. On the one hand, ultra-high data transmission rate requires a lot of available spectrum resources, and the THz band can provide an ultra-wide usable spectrum. On the other hand, since wavelengths in the THz band are short, a large number of antennas can be integrated as massive MIMO arrays to mitigate high attenuation [27]. In this way, the antenna array size is reduced as much as possible to meet the practical application requirements. With strong directionality and limited transmission distances, the THz band gains a better reputation in terms of communication security and anti-eavesdropping than lower frequencies [28].

In [29]–[31], THz channel measurement campaigns were carried out in indoor and outdoor scenarios to provide reliable channel data. To support channel simulations in THz frequencies, studies were conducted to characterize and model the channel properties [32]–[35]. Geometry-based stochastic model (GBSM) has the advantage of strong universality and can be used in multiple scenarios and frequency bands [36]. A

novel GBSM considering the diffuse scattering and molecular adsorption in the THz band was proposed in [37], in which deterministic and stochastic modeling methods were combined. Moreover, general three-dimensional (3D) THz channel modeling methods based on GBSM were discussed in [36], [38], where the non-stationarities in time, frequency, and space domains were included. In [39], a 3D double-sphere GBSM was proposed for 6G ultra massive MIMO systems. However, the channel models aforementioned excluded the consideration of non-reciprocity. Compared with the existing models, there are three aspects of improvement. First, we establish and utilize the relationship between DL and UL channels and generate correlated bidirectional channel responses simultaneously, thus reducing complexity and maintaining spatial consistency. Second, the molecular absorption and diffuse scattering are considered for each ray to fit THz propagation properties. Third, we improve the double-sphere model by adding virtual links to meet the requirement of large bandwidth.

In this paper, a 3D non-stationary and non-reciprocal GBSM for THz asymmetric massive MIMO systems is proposed, and bidirectional channel impulse responses are derived. The correlation between DL and UL channels in asymmetric massive MIMO systems is studied for the first time. Meanwhile, non-stationarities in time, frequency, and space domains are considered and modeled. The novelties and main contributions of this paper are summarized as follows.

- 1) A novel 3D non-stationary channel model is proposed for THz asymmetric massive MIMO systems. The non-reciprocity is introduced into the modeling scheme by using different beam patterns, and impact of beamwidth on channel properties is analyzed. THz propagation attenuation features are also involved and validated by measured data.
- 2) A directional effective scatterer generation (DESG) algorithm under non-reciprocal beam patterns is designed. The correlation function between UL and DL in asymmetric massive MIMO systems is derived for the first time. Computational complexity of the proposed model is reduced by considering reused scatterers.
- 3) Statistical properties that illustrate the non-reciprocity of bidirectional channels are presented. Non-stationarities in time, frequency, and space domains are validated by the corresponding correlation functions. The accuracy of the non-reciprocal channel model is validated by comparing with ray tracing data.

The rest of this paper is organized as follows. The proposed 3D non-reciprocal channel model for THz massive MIMO systems are introduced in Section II. Section III investigates the derivations of channel statistical properties of the proposed model. Next, results and validation of the proposed model are illustrated in Section IV. Finally, conclusions are drawn in Section V.

II. 3D NON-RECIPROCAL CHANNEL MODEL IN ASYMMETRIC MASSIVE MIMO SYSTEMS

An example of the asymmetric massive MIMO system configuration in the urban scenario is shown in Fig. 1. Antenna

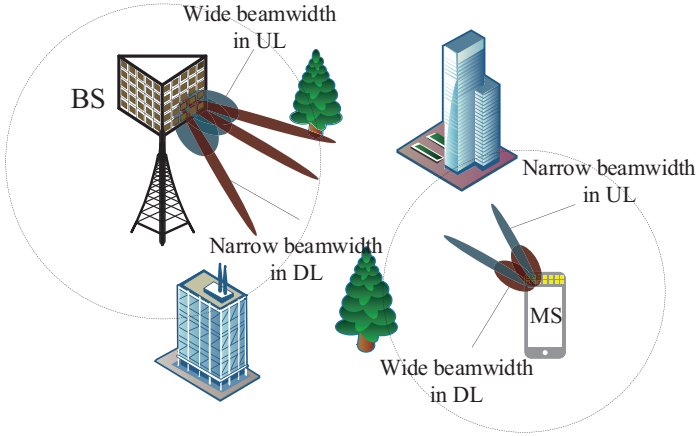


Fig. 1. Scenario configuration of the proposed 3D non-reciprocal channel model.

arrays of both BS and MS are deployed non-reciprocally. A narrow beam pattern with high gain is used for the DL channel at the BS to guarantee the communication quality. At the same time, a wide beam pattern with low gain is used for the UL at the BS, so better coverage for the MS is obtained and the complexity of beam tracking and beam management is reduced. For the MS side, small-scale non-reciprocal arrays are also used to accomplish a well-maintained link budget, i.e., a wider beamwidth for receiving and a narrower one for transmitting.

A. Model Description

The geometric relationship of the proposed 3D non-reciprocal channel model is illustrated in Fig. 2. The channel model is established based on double-sphere GBSM. Uniform rectangular arrays (URAs) are deployed at the MS side and BS side, containing P and Q elements, respectively. It should be noted that other array forms can also be applied within our model. There are P_y rows and P_z columns in the BS array, similarly, Q_y rows and Q_z columns in the MS array. The distance between two adjacent array elements in both dimensions is d , and generally $d = \lambda/2$ (λ denotes the wavelength). Therefore, the values of P , Q are given by $P = P_y \times P_z$ and $Q = Q_y \times Q_z$. It should be noted that (x_G, y_G, z_G) axes are established as the global coordinate system (GCS) with origin under the (1,1)th element of the BS array with distance H_T , representing the height of BS. Similarly, let H_R denote the MS height. We assume that the scatterers are distributed on the spheres centering on O_T and O_R at the BS side and MS side. The horizontal distance between the BS and MS is denoted as D . The MS is assumed to be movable with velocity \mathbf{V}_{MS} . For simplicity, the (1,1)th array element is located at the origin of the local coordinate system (LCS) of the BS side, and the position vector of the (p_y, p_z) th element of the BS side is given by $\mathbf{I}_T^p = [0, (p_y - 1)d, (p_z - 1)d]$.

Scatterers centered on the BS take d_T as radius, and the number of scatterers is N_T , while those centered on the MS take d_R as radius, and the number of scatterers is N_R . It is noted that the radius of scatterer sphere, which is empirically decided by propagation environment, can impact the values

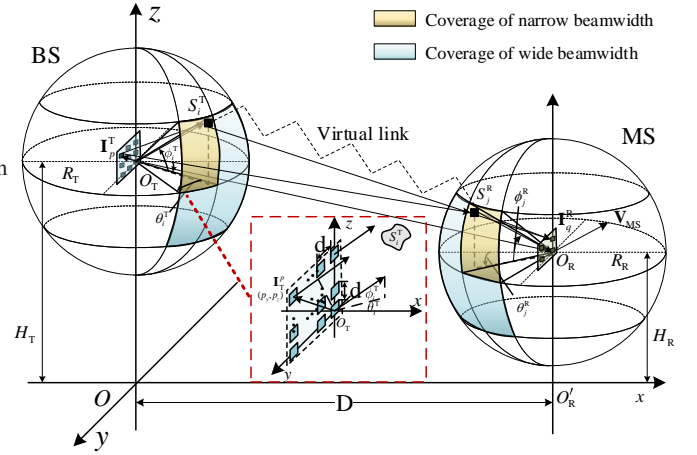


Fig. 2. Geometric relationships of the proposed 3D non-reciprocal channel model.

of ray parameters like delay and angle, but will not affect the qualitative regularity like channel correlation. Due to the non-reciprocity of the UL and DL channels, different sets of scatterers are illuminated by different antenna beams, which are defined as effective scatterers. Taking the DL as an example, let S_i^T denotes the i th effective scatterer of the BS side, and S_j^R denotes the j th effective scatterer of the MS side. Azimuth angle of departure (AAoD) corresponding to S_i^T is denoted as θ_i^D , and elevation angle of departure (EAoD) corresponding to S_i^T is denoted as ϕ_i^D . Azimuth angle of arriving (AAoA) corresponding to S_j^R is denoted as θ_j^A , and elevation angle of arriving (EAoA) corresponding to S_j^R is denoted as ϕ_j^A .

According to the geometrical relationship in Fig. 2 and the involved parameters listed in Table I, the position vector of S_i^T of the BS side centering O_T and the position vector of S_j^R of the MS side centering O_R can be expressed as

$$\begin{aligned} \mathbf{D}_{O_T}^{S_i^T}(t) &= d_T \begin{bmatrix} \cos \phi_i^D(t) \cos \theta_i^D(t) \\ \cos \phi_i^D(t) \sin \theta_i^D(t) \\ \sin \phi_i^D(t) \end{bmatrix}^T, \\ \mathbf{D}_{O_R}^{S_j^R}(t) &= d_R \begin{bmatrix} \cos \phi_j^A(t) \cos \theta_j^A(t) \\ \cos \phi_j^A(t) \sin \theta_j^A(t) \\ \sin \phi_j^A(t) \end{bmatrix}^T. \end{aligned} \quad (1)$$

Due to the mobility of the MS, the path vector of the line-of-sight (LoS) component is given by

$$\mathbf{D}^{\text{LoS}}(t) = \overrightarrow{OO_R} + \mathbf{V}_{MS} \cdot t - \overrightarrow{OO_T}. \quad (2)$$

The single bounces occur on the scatterer sphere of the BS or MS side. Path vectors of single bounce components can be expressed as

$$\begin{aligned} \mathbf{D}_{O_R}^{S_i^T}(t) &= \mathbf{D}_{O_T}^{S_i^T}(t) - \mathbf{D}^{\text{LoS}}(t), \\ \mathbf{D}_{O_T}^{S_j^R}(t) &= \mathbf{D}^{\text{LoS}}(t) + \mathbf{D}_{O_R}^{S_j^R}(t) \end{aligned} \quad (3)$$

where $\mathbf{D}_{O_R}^{S_i^T}(t)$ represents the path vector from O_R to S_i^T and $\mathbf{D}_{O_T}^{S_j^R}(t)$ represents the path vector from O_T to S_j^R . Moreover, the double bounces occur on the scatterer spheres of both BS and MS sides. A virtual link exists from S_i^T to S_j^R with delay

TABLE I
DEFINITIONS OF MAIN PARAMETERS FOR THE PROPOSED NON-RECIPROCAL CHANNEL MODEL.

Notations	Definitions
H_T, H_R	Heights of the BS and MS
D	Initial distance between the BS and MS
d_T, d_R	Radius of the scatterers sphere
κ, θ_c, ϕ_c	Concentration parameter, mean azimuth and elevation angles of the von Mises-Fisher distribution
$\mathbf{I}_T^p, \mathbf{I}_R^q$	Position vectors of the p th element of the BS side and the q th element of the MS side
$\{\theta_i^T, \phi_i^T\}, \{\theta_j^R, \phi_j^R\}$	Azimuth and elevation angles of scatterers for S_i^T and S_j^R
$\theta_{\text{pole}}, \phi_{\text{pole}}$	Planar and vertical directivity angles of the antenna beam center
α, β	Angles of planar and vertical beamwidth
$u \in \{T, R\}, \mathcal{L} \in \{DL, UL\}$	Transmitting side u and direction of link \mathcal{L}
N_u	Total number of scatterers on the u side
$C_{\text{eff}}^{u, \mathcal{L}}$	A set of effective scatterers on the u side for \mathcal{L} direction
$N_{\text{eff}}^{u, \mathcal{L}}$	Total number of effective scatterers on the u side for \mathcal{L} direction
\mathbf{V}_{MS}	Velocity vector of the MS
$\mathbf{D}_{O_T}^{S_i^T}(t), \mathbf{D}_{O_R}^{S_j^R}(t)$	Position vectors of S_i^T and S_j^R
$\mathbf{D}_p^{S_i^T}(t), \mathbf{D}_q^{S_j^R}(t)$	Path vector of the p th antenna at the BS to the scatterer S_i^T and path vector of the q th antenna at the MS to the scatterer S_j^R
$\mathbf{D}_{q,p}^{\text{LoS}}(t)$	Vector for the LoS component
$G^{\mathcal{L}}(t)$	Antenna gain for \mathcal{L} direction
$A_{q,p}^{\text{LoS}}(t), A_{q,p}^{S_i^u}(t), A_{q,p}^{S_i,j}(t)$	Attenuation of the LoS component, single bounce components, and double bounces components due to molecular absorption
$\chi^{\text{SB}}, \chi^{\text{DB}}$	Attenuation of single bounce components and double bounces components due to diffuse scattering
$\nu_{q,p}^{\text{LoS}}(t), \nu_{q,p}^{S_i^u}(t), \nu_{q,p}^{S_i,j}(t)$	Doppler frequency shift of the LoS component, single bounce components, and double bounces components

$\tilde{\tau}^{S_{i,j}}(t)$, which can be drawn by the exponential distribution as described in [40].

Fig. 2 also shows the geometric relationship between antenna array elements and scatterers at the BS side. $\mathbf{D}_p^{S_i^T}$ denotes the path vector between the p th antenna element and scatterer S_i^T of the BS side, which is calculated as

$$\mathbf{D}_p^{S_i^T}(t) = \mathbf{D}_{O_R}^{S_i^T}(t) - \mathbf{I}_T^p. \quad (4)$$

Similar relationship is to the q th element at the MS side. The path vector between the q th antenna element and scatterer S_j^R and that of the LoS component between the p th antenna element at the BS side and the q th antenna element at the MS side is given by

$$\begin{aligned} \mathbf{D}_q^{S_j^R}(t) &= \mathbf{I}_R^q - \mathbf{D}_{O_R}^{S_j^R}(t), \\ \mathbf{D}_{p,q}^{\text{LoS}}(t) &= \mathbf{D}^{\text{LoS}}(t) - \mathbf{I}_T^p + \mathbf{I}_R^q. \end{aligned} \quad (5)$$

B. Modeling of Antenna Beams

One of the most distinct properties in the asymmetric massive MIMO systems is the non-reciprocal beam patterns. According to the aforementioned double-sphere model, scatterers are randomly generated on the sphere and filtered by the directional beamwidth. Therefore, the 3D modeling strategy of the antenna beam is discussed here.

The 3D spatial antenna beam can be approximated by a pyramidal model [41] with planar and vertical angles α and β , respectively, as displayed in Fig. 3. Direction of the antenna beam center is denoted by the planar directivity angle θ_{pole} and the vertical directivity angle ϕ_{pole} . As a result, the radiation pattern can be denoted as $F(\theta_{\text{pole}}, \phi_{\text{pole}}, \alpha, \beta)$. The surface

area on the scatterer sphere that is within the coverage of the antenna beam is the area of effective scatterers, and is denoted as E_A . As α and β getting greater, the corresponding antenna beam is wider and the area of effective scatterers is larger.

C. Directional Effective Scatterer Generation Algorithm

Scatterers at the BS or MS side are distributed on a spherical surface, following the von Mises-Fisher random distribution [42], which is a directional statistic distribution that can be applied to the positions of scatterers on the surface of 3D sphere. The probability density function (PDF) of the von Mises-Fisher distribution for the random unit vector \mathbf{x} is expressed as (6), which refers to Formula(1) in [43].

$$f_p(\mathbf{x}; \boldsymbol{\mu}, \kappa) = C_p(\kappa) \exp(\kappa \boldsymbol{\mu}^T \mathbf{x}). \quad (6)$$

The parameters $\boldsymbol{\mu}$ and κ represent the mean direction vector and the concentration parameter, respectively, where $\kappa \geq 0$ and $\|\boldsymbol{\mu}\| = 1$. $\|\cdot\|$ stands for the Frobenius norm operator. In

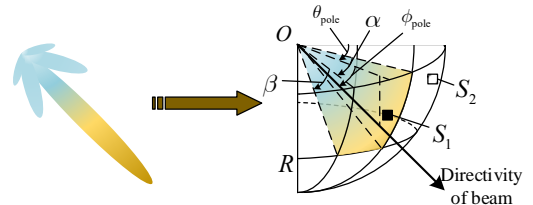


Fig. 3. Modeling of 3D spatial antenna beams.

3D application scenarios, the dimension parameter $p = 3$, and the normalization constant $C_3(\kappa)$ is expressed as

$$C_3(\kappa) = \frac{\kappa}{4\pi \sinh \kappa}. \quad (7)$$

The combination of elevation angle ϕ and azimuth angle θ specifies the position of scatterers on the spherical surface. As a result, the 3D unit vector \mathbf{x} is given by $\mathbf{x} = [\cos \phi \cos \theta, \cos \phi \sin \theta, \sin \phi]$, and the mean direction vector $\boldsymbol{\mu}$ is given by $\boldsymbol{\mu} = [\cos \phi_0 \cos \theta_0, \cos \phi_0 \sin \theta_0, \sin \phi_0]$. As the value of κ gets greater, the scatterers are more concentrated on $\boldsymbol{\mu}$ along the spherical surface.

Scatterers randomly distributed on the spherical surface can be regarded as effective scatterers only if they are located in the area of E_A . For example, two scatterers, S_1 and S_2 , are distributed on the spherical surface in Fig. 3, but only S_1 is counted as an effective scatterer and contributes to the channel response because S_1 locates on E_A , while S_2 does not. The set of effective scatterers is denoted as C_{eff} . The whole process of the DESG algorithm is shown in Algorithm 1.

Algorithm 1: DESG algorithm in asymmetric massive MIMO systems

```

1 Generate scatterers of both sides according to
  parameters  $\kappa$ ,  $\theta_0$ , and  $\phi_0$  in von Mises-Fisher
  distribution.
2 foreach  $\mathcal{L} \in \{\text{DL}, \text{UL}\}$  do
3   foreach  $u \in \{\text{T}, \text{R}\}$  do
4     Determine the area of effective scatterers  $E_{A,u}^{\mathcal{L}}$ ;
5      $i = 1$ ;
6     while  $i \leq N_u^{\mathcal{L}}$  do
7       if  $\theta_i^{u,\mathcal{L}} \in \left[ \theta_{u,\mathcal{L}}^{\text{B}} - \frac{\alpha_{\mathcal{L}}}{2}, \theta_{u,\mathcal{L}}^{\text{B}} + \frac{\alpha_{\mathcal{L}}}{2} \right]$  and
8          $\phi_i^{u,\mathcal{L}} \in \left[ \phi_{u,\mathcal{L}}^{\text{B}} - \frac{\beta_{\mathcal{L}}}{2}, \phi_{u,\mathcal{L}}^{\text{B}} + \frac{\beta_{\mathcal{L}}}{2} \right]$  then
9            $S_i^u$  is accounted as an effective
10          scatterer.
11         else
12            $S_i^u$  is excluded out of effective
13          scatterers.
14         end
15        $i = i + 1$ ;
16     end
17   end
18 end
19 The sets of effective scatterers  $C_{\text{eff}}^{\text{T,DL}}$ ,  $C_{\text{eff}}^{\text{T,UL}}$ ,  $C_{\text{eff}}^{\text{R,DL}}$ ,
20 and  $C_{\text{eff}}^{\text{R,UL}}$  are assembled.

```

Moreover, in real communication conditions, it is unreasonable to assume that the DL and UL channels are completely independent. Since the BS and MS are located in the same scenario and the antenna beams have overlapping areas, some electromagnetic waves will experience the same propagation process. Thus, the DL and UL channels are correlated more or less. By reusing the scatterers of narrow beamwidth side, the correlation between DL and UL can be introduced. For instance, the effective scatterers of the BS side in DL are determined by the narrow beamwidth, which are included in the effective scatterers corresponding to the wide beamwidth in

UL. Therefore, the effective scatterers in the overlapped area, i.e., the area of narrow beamwidth in DL at the BS side, can be reused in the other direction. The same is to the generation of effective scatterers of the MS side. Moreover, the approach of reusing the effective scatterers reduces the computation cost, which is verified in Section IV-D.

D. THz Propagation Attenuation Properties

Apart from the inevitable free-space path loss, there are two kinds of propagation attenuation properties in the THz band which are quite disparate from those of the low-frequency waves, i.e., the molecular absorption and the diffuse scattering due to rough surfaces [44], [45]. In order to accurately simulate the attenuation of THz channel, we embed these two propagation characteristics into the model and compare and verify with the measured data. First, the THz waves resonate with molecules like oxygen and water in the air, which leads to vast energy loss called the molecular absorption attenuation. The frequency-selective absorption peaks split the spectrum into several transmission windows [37]. The molecular absorption attenuation is discussed together with the free-space propagation in Section II-D. Second, diffuse scattering occurs when THz waves are incident on the material whose roughness is comparable to the wavelength, and losses in the diffuse scattering process are considerable [46]. Molecular absorption attenuation and diffuse scattering attenuation play a crucial role in the THz propagation and should be considered.

Here, we briefly analyze the diffuse scattering attenuation. Wavelengths of THz waves are very short, which are comparable to the roughness of surfaces with which to interact. Therefore, the non-line-of-sight (NLoS) path components experience significant diffuse scattering attenuation in the THz band. N_ϵ kinds of scatterers are considered to be distributed in the environment. For the ϵ th ($\epsilon = 1, \dots, N_\epsilon$) kind of scatterer, the probability of occurrence is P_ϵ . The corresponding rough surface root mean square (RMS) height is given by $\rho_{h,\epsilon}$, and the index of refraction is $n_{t,\epsilon}$.

The NLoS paths can be divided into three categories, i.e., reflection, scattering, and diffraction. In the THz band, attenuation of the diffraction is much lower than the other two, so that its influence can be ignored [46]. When a beam of THz wave is incident on a rough surface as depicted in Fig. 4(a), the incident wave becomes either reflected or scattered wave. Accordingly, the simplified geometric relationship of the diffuse scattering is illustrated in Fig. 4(b). The coordinate axis is established as the LCS of the rough surface, in which θ_{in} denotes the incident angle, θ_{out} and φ_{sca} are elevation and azimuth angles of the scattered wave, respectively.

Let χ_{ref} and χ_{sca} denote reflection attenuation and diffuse scattering coefficient, respectively. When $\theta_{\text{in}} = \theta_{\text{out}}$ and $\varphi_{\text{sca}} = 0$, reflection occurs on the rough surface. According to Kirchoff scattering theory, the reflection coefficient χ_{ref} can be calculated as [47]

$$\chi_{\text{ref}} = \text{Fr} \times \rho_r \quad (8)$$

where Fr denotes the Fresnel reflection coefficient and ρ_r denotes Rayleigh roughness factor, which are calculated by

$$Fr = \frac{\cos \theta_{in} - n_t \sqrt{1 - (n_t^{-1} \sin \theta_{in})^2}}{\cos \theta_{in} + n_t \sqrt{1 - (n_t^{-1} \sin \theta_{in})^2}}, \quad (9)$$

$$\rho_r = \exp \left[-8 \left(\frac{\pi \rho_h \cos \theta_{in}}{\lambda} \right)^2 \right]$$

where n_t is the index of refraction, ρ_h is the RMS height of rough surface, and λ is the wavelength.

When $\theta_{in} \neq \theta_{out}$ or $\varphi_{sca} \neq 0$, diffuse scattering is observed on the rough surface. The scattering coefficient χ_{sca} can be calculated by [47]

$$\chi_{sca} = Fr \times \rho_s \quad (10)$$

where ρ_s is the scattering loss factor, which can be referred to [48].

In the modeling process, each effective scatterer position is assigned a kind of material according to P_ϵ . Then, the orientation of the rough surface in each position is randomly generated, and each ray is classified as either scattered or reflected by its angles. At last, the attenuation coefficient is calculated and multiplied in the channel impulse response.

Here, we validate the combined THz propagation properties. In [31], THz channel measurement campaign was carried out at 140 GHz central frequency in urban scenario under the LoS condition, which is chosen as the comparison standard. Simulations are conducted with the same configurations as described in [31]. Comparison of path losses between the BS and MS is shown in Fig. 5. It can be illustrated that the proposed model has a good ability to depict channel fading characteristics in the THz band.

E. Bidirectional Channel Impulse Response (CIR) and Transfer Function

Based on the double-sphere model structure and the DESG algorithm aforementioned, bidirectional CIRs are derived. The impulse responses of DL and UL channels can be generated at the same time, and the difference between them is that the visible scatterers generated and matched according to the DESG algorithm are different. The detailed derivation is as follows.

The proposed non-reciprocal channel model can be characterized by two $P \times Q$ matrices $\mathbf{H}^\mathcal{L}(t, \tau) = [h_{q,p}^\mathcal{L}(t, \tau)]_{P \times Q}$ for P antenna elements of the MS side and Q of the BS side. \mathcal{L} represents the direction of current link, $\mathcal{L} = DL$

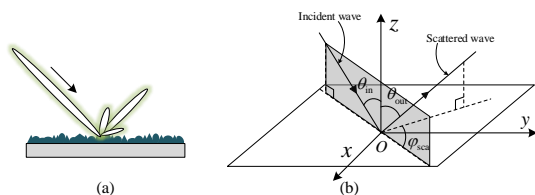


Fig. 4. Illustrations of the diffuse scattering in THz band. (a) Schematic diagram of the THz wave incidence; and (b) geometric relationship of the incident and scattered waves.

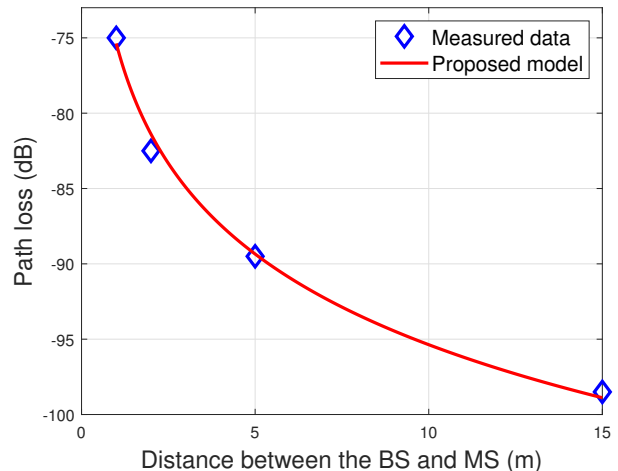


Fig. 5. Comparison of the measured data and the proposed model with respect to path loss in DL ($f = 140$ GHz, $D = 1$ m-15 m, $H_T = 1.65$ m, $H_R = 1.65$ m, $R_T = 10$ m, $N_T = 50$, $R_R = 5$ m, $N_R = 100$, $[\alpha_R^{DL}, \beta_R^{DL}] = [\pi/3, \pi/4]$, $[\alpha_T^{DL}, \beta_T^{DL}] = [\pi/6, \pi/6]$).

for downlink, and $\mathcal{L} = UL$ for uplink, i.e., $\mathcal{L} \in \{DL, UL\}$. Also, p represents the p th antenna element of the BS side, \mathbf{I}_T^p denotes the position vector of the p th antenna element in LCS, and the same is to antenna elements of the MS side. In the established THz communication scenario, scatterers abound on both sides, as a result, received signal contains also NLoS paths such as single bounce paths and double bounces paths, in addition to the LoS path that occupies most of the power. Diffuse scattering attenuation of each bounce is in tens of dB, which yields a considerable impact on the signal strength of multi-bounce paths. Consequently, NLoS paths with more than double bounces could be left out of consideration [38].

$h_{q,p}^\mathcal{L}(t, \tau)$ is composed of the LoS path and NLoS paths, and is expressed as

$$h_{q,p}^\mathcal{L}(t, \tau) = h_{q,p}^{\text{LoS}, \mathcal{L}}(t, \tau) + h_{q,p}^{\text{NLoS}, \mathcal{L}}(t, \tau) \quad (11)$$

where $h_{q,p}^{\text{NLoS}, \mathcal{L}}(t, \tau)$ can be further expressed as

$$\begin{aligned} h_{q,p}^{\text{NLoS}, \mathcal{L}}(t, \tau) &= h_{q,p}^{\text{SB}_T, \mathcal{L}}(t, \tau) + h_{q,p}^{\text{SB}_R, \mathcal{L}}(t, \tau) + h_{q,p}^{\text{DB}, \mathcal{L}}(t, \tau) \\ &= \sum_{u \in \{T, R\}} h_{q,p}^{\text{SB}_u, \mathcal{L}}(t, \tau) + h_{q,p}^{\text{DB}, \mathcal{L}}(t, \tau). \end{aligned} \quad (12)$$

In (12), superscript $\text{SB}_u (u \in \{T, R\})$ denotes a NLoS path with single bounce on u side, within which, $u = T$ for the MS, and $u = R$ for the BS. Superscript DB denotes a NLoS path with double bounce whose scatterers are on both sides. For the LoS component, $h_{q,p}^{\text{LoS}, \mathcal{L}}(t, \tau)$ can be calculated by (13), where $k = 2\pi/\lambda$ is the wavenumber. $G^\mathcal{L}(t)$ is the antenna gain, and its detailed calculation is presented in Appendix A. $A_{q,p}^{\text{LoS}}(t)$ represents the attenuation due to free-space propagation and molecular absorption, and the detailed calculation is presented in Appendix B, where distance d that the ray travels should be replaced by the total distance $d^{\text{LoS}} = \|\mathbf{D}^{\text{LoS}}(t)\|$.

The calculation of phase shift $\Phi_{q,p}^{\text{LoS}}(t)$ under SWM is given by

$$\Phi_{q,p}^{\text{LoS}}(t) = \Phi_0^{\text{LoS}} + k \|\mathbf{D}_{p,q}^{\text{LoS}}(t)\| \quad (14)$$

$$h_{q,p}^{\text{LoS},\mathcal{L}}(t, \tau) = \bar{h}_{q,p}^{\text{LoS},\mathcal{L}}(t) \delta(\tau - \tau_{q,p}^{\text{LoS}}(t)) = \sqrt{A_{q,p}^{\text{LoS}}(t) G^{\mathcal{L}}(t)} e^{j\Phi_{q,p}^{\text{LoS}}} e^{j2\pi\nu_{q,p}^{\text{LoS}}(t)t} \delta(\tau - \tau_{q,p}^{\text{LoS}}(t)) \quad (13)$$

where Φ_0^{LoS} is a random phase variable uniformly distributed within $(0, 2\pi]$. The Doppler frequency shift $\nu^{\text{LoS}}(t)$ of the LoS component is given by

$$\nu_{q,p}^{\text{LoS}}(t) = \frac{\|\mathbf{V}_{\text{MS}}\| \langle -\mathbf{D}_{p,q}^{\text{LoS}}(t), \mathbf{V}_{\text{MS}} \rangle}{\lambda \|\mathbf{D}_{p,q}^{\text{LoS}}(t)\| \|\mathbf{V}_{\text{MS}}\|} = \frac{\langle -\mathbf{D}_{p,q}^{\text{LoS}}(t), \mathbf{V}_{\text{MS}} \rangle}{\lambda \|\mathbf{D}_{p,q}^{\text{LoS}}(t)\|} \quad (15)$$

where $\langle \cdot, \cdot \rangle$ is the inner product operator. $\tau_{q,p}^{\text{LoS}}(t)$ represents the propagation delay between the the BS and MS, which is calculated by

$$\tau_{q,p}^{\text{LoS}}(t) = \frac{\|\mathbf{D}_{p,q}^{\text{LoS}}(t)\|}{c}. \quad (16)$$

For the NLoS components, the CIR of single bounce paths $h_{q,p}^{\text{SB}_u,\mathcal{L}}(t, \tau)$ can be calculated by (17), where $S_i^u \in C_{\text{eff}}^{u,\mathcal{L}}$ represents the i th effective scatterer for \mathcal{L} direction of u side, whose total number is $N_{u,\text{eff}}^{\mathcal{L}}$. Calculation of the antenna gain $G^{\mathcal{L}}(t)$ follows the same procedure as that of the LoS component, which is presented in Appendix A. $A_{q,p}^{S_i^u}$ is the attenuation due to free-space propagation combined with molecular absorption, which can be calculated according to Appendix B. Distance d that the ray travels should be replaced by the total distance of two parts, a part from the transmitting antenna to the scatterer and a part from the scatterer to the receiving antenna, i.e., $d^{\text{SB}_u} = \|\mathbf{D}_p^{S_i^u}(t)\| + \|\mathbf{D}_q^{S_i^u}(t)\|$. The diffuse scattering attenuation of paths with single bounce is χ^{SB} , and the detailed calculation has already been elaborated in Section II-D.

The phase shift $\Phi_{q,p}^{S_i^u}(t)$ under SWM is given by

$$\Phi_{q,p}^{S_i^u}(t) = \Phi_0^{\text{SB}_u} + k \left(\|\mathbf{D}_p^{S_i^u}(t)\| + \|\mathbf{D}_q^{S_i^u}(t)\| \right) \quad (18)$$

where $\Phi_0^{\text{SB}_u}$ is a random phase variable uniformly distributed within $(0, 2\pi]$. The Doppler frequency shift $\nu_{q,p}^{S_i^u}(t)$ of the single bounce component is given by

$$\nu_{q,p}^{S_i^u}(t) = \frac{\|\mathbf{V}_{\text{MS}}\| \langle -\mathbf{D}_q^{S_i^u}(t), \mathbf{V}_{\text{MS}} \rangle}{\lambda \|\mathbf{D}_q^{S_i^u}(t)\| \|\mathbf{V}_{\text{MS}}\|} = \frac{\langle -\mathbf{D}_q^{S_i^u}(t), \mathbf{V}_{\text{MS}} \rangle}{\lambda \|\mathbf{D}_q^{S_i^u}(t)\|}. \quad (19)$$

$\tau_{q,p}^{S_i^u}(t)$ represents the delay of single bounce component, which is calculated by

$$\tau_{q,p}^{S_i^u}(t) = \frac{\|\mathbf{D}_p^{S_i^u}(t)\| + \|\mathbf{D}_q^{S_i^u}(t)\|}{c}. \quad (20)$$

Moreover, the CIR of double bounce paths $h_{q,p}^{\text{DB},\mathcal{L}}(t, \tau)$ can be calculated by (21), where $S_i^T \in C_{\text{eff}}^{T,\mathcal{L}}, S_j^R \in C_{\text{eff}}^{R,\mathcal{L}}$ represent the effective scatterers for both directions. $N_{T,\text{eff}}^{\mathcal{L}}$ and $N_{R,\text{eff}}^{\mathcal{L}}$ are the numbers of effective scatterers for \mathcal{L} direction of the BS and MS side, respectively. Calculation of the antenna gain $G^{\mathcal{L}}(t)$ follows the same procedure to that of the LoS component, which is presented in Appendix A. $A_{q,p}^{S_i^T, S_j^R}(t)$ is the attenuation due to free-space propagation combined with molecular absorption, and can be calculated according to Appendix B. Distance d that the ray travels should be

replaced by the total distance of three parts, a part from the transmitting antenna to the scatterer, a part from the scatterer to the receiving antenna, and the last part of virtual links, i.e., $d^{\text{DB}} = \|\mathbf{D}_p^{S_i^T}(t)\| + \|\mathbf{D}_q^{S_j^R}(t)\| + \|\tilde{\tau}^{S_i^T, S_j^R}(t) \cdot c\|$. The diffuse scattering attenuation of paths with double bounces is χ^{DB} , and its approximate calculation is given by $\chi^{\text{DB}} = (\chi^{\text{SB}})^2$.

Phase shift $\Phi_{q,p}^{S_i^T, S_j^R}(t)$ under SWM is given by

$$\Phi_{q,p}^{S_i^T, S_j^R}(t) = \Phi_0^{\text{DB}} + k \left(\|\mathbf{D}_p^{S_i^T}(t)\| + \|\mathbf{D}_q^{S_j^R}(t)\| + \|\tilde{\tau}^{S_i^T, S_j^R}(t) \cdot c\| \right) \quad (22)$$

where Φ_0^{DB} is a random phase variable uniformly distributed within $(0, 2\pi]$. The Doppler frequency $\nu_{q,p}^{S_i^T, S_j^R}(t)$ of the double bounce component is given by

$$\nu_{q,p}^{S_i^T, S_j^R}(t) = \frac{\|\mathbf{V}_{\text{MS}}\| \langle -\mathbf{D}_q^{S_j^R}(t), \mathbf{V}_{\text{MS}} \rangle}{\lambda \|\mathbf{D}_q^{S_j^R}(t)\| \|\mathbf{V}_{\text{MS}}\|} = \frac{\langle -\mathbf{D}_q^{S_j^R}(t), \mathbf{V}_{\text{MS}} \rangle}{\lambda \|\mathbf{D}_q^{S_j^R}(t)\|}. \quad (23)$$

$\tau_{q,p}^{S_i^T, S_j^R}(t)$ represents the delay of double bounce NLoS component, which is given by

$$\tau_{q,p}^{S_i^T, S_j^R}(t) = \frac{\|\mathbf{D}_p^{S_i^T}(t)\| + \|\mathbf{D}_q^{S_j^R}(t)\| + \|\tilde{\tau}^{S_i^T, S_j^R}(t) \cdot c\|}{c}. \quad (24)$$

The channel transfer functions of both directions $H_{q,p}^{\mathcal{L}}(t, f)$ can be derived by applying Fourier transform to the CIR with respect to delay τ , which can be expressed in (25). In the THz band, the communication bandwidth is extremely large, so the influence of frequency on channel fading should be taken into account by adding a correction factor [49], [50]. Typically, this can be modeled by frequency-dependent path gain $(f/f_c)^{\gamma_k}$ [40], where γ_k represents the environment-dependent random variable, and the channel transfer function can be rewritten as (26).

According to the above modeling principles, the complete flow chart is shown in Fig. 6.

III. STATISTICAL PROPERTIES

In this section, we derive key channel statistics that characterize the non-reciprocity and non-stationarities of the proposed model, including correlation functions of UL and DL and in time, frequency, and space domains.

A. Correlation Functions of UL and DL

The correlation function between both directions can reflect the degree of channel correlation affected by beamwidth and environmental changes, which can be calculated as

$$\rho_{q,p}(t_0) = \mathbb{E}[\bar{h}_{q,p}^{\text{DL}}(t_0) \bar{h}_{q,p}^{\text{UL}*}(t_0)] = \rho_{q,p}^{\text{LoS}}(t_0) + \rho_{q,p}^{\text{SB}}(t_0) + \rho_{q,p}^{\text{DB}}(t_0). \quad (27)$$

It is noted that the computation of the correlation function is not strictly at the same time. The switching of UL and DL communications is done by a radio frequency electromagnetic switch, and the switching time is within $1 \mu\text{s}$, which is

$$\begin{aligned}
 h_{q,p}^{SB,u,\mathcal{L}}(t, \tau) &= \sum_{S_i^u \in C_{\text{eff}}^{u,\mathcal{L}}} \bar{h}_{q,p}^{S_i^u,\mathcal{L}}(t) \delta(\tau - \tau_{q,p}^{S_i^u}(t)) = \frac{\sqrt{\chi^{SB}}}{\sqrt{N_{u,\text{eff}}^{\mathcal{L}}}} \sum_{S_i^u \in C_{\text{eff}}^{u,\mathcal{L}}} \sqrt{A_{q,p}^{S_i^u}(t) G^{\mathcal{L}}(t)} e^{j\Phi_{q,p}^{S_i^u}(t)} e^{j2\pi\nu_{q,p}^{S_i^u}(t)t} \delta(\tau - \tau_{q,p}^{S_i^u}(t)) \quad (17) \\
 h_{q,p}^{DB,\mathcal{L}}(t, \tau) &= \sum_{S_i^T \in C_{\text{eff}}^{T,\mathcal{L}}} \sum_{S_j^R \in C_{\text{eff}}^{R,\mathcal{L}}} \bar{h}_{q,p}^{S_i^T, S_j^R,\mathcal{L}}(t) \delta(\tau - \tau_{q,p}^{S_i^T, S_j^R}(t)) \\
 &= \frac{\sqrt{\chi^{DB}}}{\sqrt{N_{T,\text{eff}}^{\mathcal{L}} N_{R,\text{eff}}^{\mathcal{L}}}} \sum_{S_i^T \in C_{\text{eff}}^{T,\mathcal{L}}} \sum_{S_j^R \in C_{\text{eff}}^{R,\mathcal{L}}} \sqrt{A_{q,p}^{S_i^T, S_j^R}(t) G^{\mathcal{L}}(t)} e^{j\Phi_{q,p}^{S_i^T, S_j^R}(t)} e^{j2\pi\nu_{q,p}^{S_i^T, S_j^R}(t)t} \delta(\tau - \tau_{q,p}^{S_i^T, S_j^R}(t)) \quad (21)
 \end{aligned}$$

$$\begin{aligned}
 H_{q,p}^{\mathcal{L}}(t, f) &= \int_{-\infty}^{\infty} h_{q,p}^{\mathcal{L}}(t, \tau) e^{-j2\pi f\tau} d\tau = H_{q,p}^{\text{LoS},\mathcal{L}}(t, f) + H_{q,p}^{\text{NLoS},\mathcal{L}}(t, f) \\
 &= \bar{h}_{q,p}^{\text{LoS},\mathcal{L}}(t) e^{-j2\pi f\tau_{q,p}^{\text{LoS}}(t)} + \sum_{u \in \{T,R\}} \sum_{S_i^u \in C_{\text{eff}}^{u,\mathcal{L}}} \bar{h}_{q,p}^{S_i^u,\mathcal{L}}(t) e^{-j2\pi f\tau_{q,p}^{S_i^u}(t)} + \sum_{S_i^T \in C_{\text{eff}}^{T,\mathcal{L}}} \sum_{S_j^R \in C_{\text{eff}}^{R,\mathcal{L}}} \bar{h}_{q,p}^{S_i^T, S_j^R,\mathcal{L}}(t) e^{-j2\pi f\tau_{q,p}^{S_i^T, S_j^R}(t)} \quad (25) \\
 H_{q,p}^{\text{NLoS},\mathcal{L}}(t, f) &= \sum_{u \in \{T,R\}} \sum_{S_i^u \in C_{\text{eff}}^{u,\mathcal{L}}} \bar{h}_{q,p}^{S_i^u,\mathcal{L}}(t, \tau) \left(\frac{f}{f_c}\right)^{\gamma_i} e^{-j2\pi f\tau_{q,p}^{S_i^u}(t)} + \sum_{S_i^T \in C_{\text{eff}}^{T,\mathcal{L}}} \sum_{S_j^R \in C_{\text{eff}}^{R,\mathcal{L}}} \bar{h}_{q,p}^{S_i^T, S_j^R,\mathcal{L}}(t, \tau) \left(\frac{f}{f_c}\right)^{\gamma_{i,j}} e^{-j2\pi f\tau_{q,p}^{S_i^T, S_j^R}(t)} \quad (26)
 \end{aligned}$$

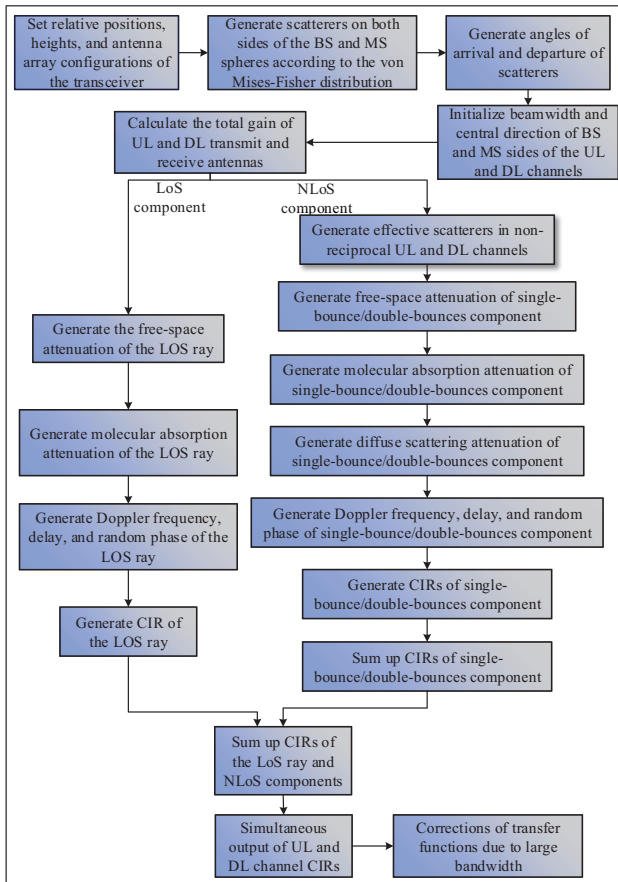


Fig. 6. Flow chart of the proposed 3D THz non-reciprocal channel model.

far shorter than the channel coherence time. Therefore, we consider the channel to be static during the switching time.

The correlation of the LoS component $\rho_{q,p}^{\text{LoS}}(t_0)$ can be

derived by

$$\begin{aligned}
 \rho_{q,p}^{\text{LoS}}(t_0) &= \mathbb{E}[\bar{h}_{q,p}^{\text{LoS,DL}}(t_0) \bar{h}_{q,p}^{\text{LoS,UL}*}(t_0)] \quad (28) \\
 &= A_{\text{LoS}}(t_0) \sqrt{G^{\text{DL}}(t_0) G^{\text{UL}}(t_0)} = \Xi(t_0) A_{\text{LoS}}(t_0)
 \end{aligned}$$

where $\Xi(t_0) = \sqrt{G^{\text{DL}}(t_0) G^{\text{UL}}(t_0)}$. The correlation of the LoS component is maintained at a constant 1 after the normalization process, which indicates the correlation of the LoS component can be dropped out of consideration.

Correlation of the single bounce component $\rho_{q,p}^{\text{SB}}(t_0)$ can be derived by (29). The calculation has been simplified due to non-correlation between paths via scatterers at the MS side and BS side. In (29), $N_{\nu_1} = \frac{1}{\sqrt{N_{T,\text{eff}}^{\text{DL}} N_{T,\text{eff}}^{\text{UL}}}}$ and $N_{\nu_2} = \frac{1}{\sqrt{N_{R,\text{eff}}^{\text{DL}} N_{R,\text{eff}}^{\text{UL}}}}$. The set of partial-effective scatterers ΔC_{eff}^u is derived by $\Delta C_{\text{eff}}^{\text{T}} = (C_{\text{eff}}^{\text{T,UL}} - C_{\text{eff}}^{\text{T,DL}})$ and $\Delta C_{\text{eff}}^{\text{R}} = (C_{\text{eff}}^{\text{R,DL}} - C_{\text{eff}}^{\text{R,UL}})$, whose numbers are calculated by $\Delta N_{\text{eff}}^{\text{T}} = \text{Card}(\Delta C_{\text{eff}}^{\text{T}})$ and $\Delta N_{\text{eff}}^{\text{R}} = \text{Card}(\Delta C_{\text{eff}}^{\text{R}})$. In the current non-reciprocal configuration, the beamwidth of UL is greater than that of DL at the BS side, so $C_{\text{eff}}^{\text{T,UL}} \in C_{\text{eff}}^{\text{T,DL}}$ is satisfied. The opposite relationship of beamwidth between DL and UL is discovered at the MS side, so $C_{\text{eff}}^{\text{R,UL}} \in C_{\text{eff}}^{\text{R,DL}}$ is satisfied. $f_3(\theta, \phi)$ denotes the PDF of the von Mises-Fisher distribution. Moreover, correlation of the double bounces component $\rho_{q,p}^{\text{DB}}(t_0)$ can be calculated by (30), where $N_\nu = N_{\nu_1} \times N_{\nu_2} = \frac{1}{\sqrt{N_{T,\text{eff}}^{\text{DL}} N_{T,\text{eff}}^{\text{UL}} N_{R,\text{eff}}^{\text{DL}} N_{R,\text{eff}}^{\text{UL}}}}$.

B. Correlations in Time, Frequency, and Space Domains

Non-stationarities of the proposed model can be reflected by the correlation functions in time, frequency, and space domains [51]. The space-time-frequency correlation function $R_{q,p;\Delta q,\Delta p}^{\mathcal{L}}(t, f; \Delta t, \Delta f)$ can be divided into three parts, i.e., a part of the LoS path $R_{q,p;\Delta q,\Delta p}^{\text{LoS},\mathcal{L}}(t, f; \Delta t, \Delta f)$, a part of NLoS paths with single bounce $R_{q,p;\Delta q,\Delta p}^{\text{SB},\mathcal{L}}(t, f; \Delta t, \Delta f)$, and a part of NLoS paths with double bounces $R_{q,p;\Delta q,\Delta p}^{\text{DB},\mathcal{L}}(t, f; \Delta t, \Delta f)$,

$$\begin{aligned}
\rho_{q,p}^{\text{SB}}(t_0) &= \mathbb{E}[\bar{h}_{q,p}^{\text{SB}_T, \text{DL}}(t_0)\bar{h}_{q,p}^{\text{SB}_R, \text{UL}*}(t_0)] + \mathbb{E}[\bar{h}_{q,p}^{\text{SB}_{R, \text{DL}}}(t_0)\bar{h}_{q,p}^{\text{SB}_{R, \text{UL}*}}(t_0)] \\
&= \Xi(t_0)\chi^{\text{SB}} \int_{-\pi}^{\pi} \int_{-\frac{\pi}{2}}^{\frac{\pi}{2}} N_{\nu_1} \left\{ N_{T, \text{eff}}^{\text{DL}} \sum_{S_i^T \in C_{\text{eff}}^{\text{T,DL}}} \left[A_{q,p}^{S_i^T}(t_0) \right] + \sum_{S_i^T \in \Delta C_{\text{eff}}^{\text{T}}} \left[A_{q,p}^{S_i^T}(t_0) e^{-j\Phi_{q,p}^{S_i^T}(t_0)} e^{-jk\nu_{q,p}^{S_i^T}(t_0)t_0} \right] \right\} f_3(\theta^T, \phi^T) d\theta^T d\phi^T \\
&+ \Xi(t_0)\chi^{\text{SB}} \int_{-\pi}^{\pi} \int_{-\frac{\pi}{2}}^{\frac{\pi}{2}} N_{\nu_2} \left\{ N_{R, \text{eff}}^{\text{UL}} \sum_{S_i^R \in C_{\text{eff}}^{\text{R,DL}}} \left[A_{q,p}^{S_i^R}(t_0) \right] + \sum_{S_i^R \in \Delta C_{\text{eff}}^{\text{R}}} \left[A_{q,p}^{S_i^R}(t_0) e^{-j\Phi_{q,p}^{S_i^R}(t_0)} e^{-jk\nu_{q,p}^{S_i^R}(t_0)t_0} \right] \right\} f_3(\theta^R, \phi^R) d\theta^R d\phi^R
\end{aligned} \tag{29}$$

$$\begin{aligned}
\rho_{q,p}^{\text{DB}}(t_0) &= \mathbb{E}[\bar{h}_{q,p}^{\text{DB}, \text{DL}}(t_0)\bar{h}_{q,p}^{\text{DB}, \text{UL}*}(t_0)] = \Xi(t_0)\chi^{\text{DB}} \int_{-\pi}^{\pi} \int_{-\pi}^{\pi} \int_{-\frac{\pi}{2}}^{\frac{\pi}{2}} \int_{-\frac{\pi}{2}}^{\frac{\pi}{2}} N_{\nu} \left\{ N_{T, \text{eff}}^{\text{DL}} N_{R, \text{eff}}^{\text{UL}} \sum_{S_i^T \in C_{\text{eff}}^{\text{T,DL}}} \sum_{S_j^R \in C_{\text{eff}}^{\text{R,UL}}} \left[A_{q,p}^{S_i, j}(t_0) \right] \right. \\
&+ \sum_{S_{i1}^T \in C_{\text{eff}}^{\text{T,DL}}} \sum_{S_{i2}^T \in \Delta C_{\text{eff}}^{\text{T}}} \sum_{S_j^R \in C_{\text{eff}}^{\text{R,UL}}} \left[\sqrt{A_{q,p}^{S_{i1}, j}(t_0) A_{q,p}^{S_{i2}, j}(t_0)} e^{j(\Phi_{q,p}^{S_{i1}, j}(t_0) - \Phi_{q,p}^{S_{i2}, j}(t_0))} \right] \\
&+ \sum_{S_i^T \in C_{\text{eff}}^{\text{T,DL}}} \sum_{S_{j1}^R \in \Delta C_{\text{eff}}^{\text{R}}} \sum_{S_{j2}^R \in C_{\text{eff}}^{\text{R,UL}}} \left[\sqrt{A_{q,p}^{S_i, j1}(t_0) A_{q,p}^{S_i, j2}(t_0)} e^{j(\Phi_{q,p}^{S_i, j1}(t_0) - \Phi_{q,p}^{S_i, j2}(t_0))} e^{jk(\nu_{q,p}^{S_i, j1}(t_0) - \nu_{q,p}^{S_i, j2}(t_0))t_0} \right] \\
&+ \sum_{S_{i1}^T \in C_{\text{eff}}^{\text{T,DL}}} \sum_{S_{i2}^T \in \Delta C_{\text{eff}}^{\text{T}}} \sum_{S_{j1}^R \in C_{\text{eff}}^{\text{R,UL}}} \sum_{S_{j2}^R \in \Delta C_{\text{eff}}^{\text{R}}} \left[\sqrt{A_{q,p}^{S_{i1}, j2}(t_0) A_{q,p}^{S_{i2}, j1}(t_0)} e^{j(\Phi_{q,p}^{S_{i1}, j2}(t_0) - \Phi_{q,p}^{S_{i2}, j1}(t_0))} \right. \\
&\left. e^{jk(\nu_{q,p}^{S_{i1}, j2}(t_0) - \nu_{q,p}^{S_{i2}, j1}(t_0))t_0} \right] \left. \right\} f_3(\theta^T, \phi^T) f_3(\theta^R, \phi^R) d\theta^T d\phi^T d\theta^R d\phi^R
\end{aligned} \tag{30}$$

which is expressed in (31).

$$\begin{aligned}
R_{q,p; \Delta q, \Delta p}^{\mathcal{L}}(t, f; \Delta t, \Delta f) \\
&= \mathbb{E}[H_{q,p}^{\mathcal{L}*}(t, f) H_{q+\Delta q, p+\Delta p}^{\mathcal{L}}(t+\Delta t, f+\Delta f)] \\
&= R_{q,p; \Delta q, \Delta p}^{\text{LoS}, \mathcal{L}}(t, f; \Delta t, \Delta f) + R_{q,p; \Delta q, \Delta p}^{\text{SB}, \mathcal{L}}(t, f; \Delta t, \Delta f) \\
&+ R_{q,p; \Delta q, \Delta p}^{\text{DB}, \mathcal{L}}(t, f; \Delta t, \Delta f)
\end{aligned} \tag{31}$$

First, to access the characteristics of correlation at different time instants, the correlation function in the time domain is used. Three parts of the correlation function at different instants on direction \mathcal{L} can be calculated by (32)–(34), where the same frequency and the same antenna pair are required, and $\Omega_{t,1} = f(\tau_{q,p}^{\text{LoS}, \mathcal{L}}(t) - \tau_{q+\Delta q, p+\Delta p}^{\text{LoS}, \mathcal{L}}(t+\Delta t))$, $\Omega_{t,2} = f(\tau_{q,p}^{S_i^u, \mathcal{L}}(t) - \tau_{q+\Delta q, p+\Delta p}^{S_i^u, \mathcal{L}}(t+\Delta t))$, $\Omega_{t,3} = f(\tau_{q,p}^{S_i, j, \mathcal{L}}(t) - \tau_{q+\Delta q, p+\Delta p}^{S_i, j, \mathcal{L}}(t+\Delta t))$ is satisfied.

$$R_{q,p}^{\text{LoS}, \mathcal{L}}(t, f; \Delta t) = \mathbb{E}[\bar{h}_{q,p}^{\text{LoS}, \mathcal{L}*}(t)\bar{h}_{q,p}^{\text{LoS}, \mathcal{L}}(t+\Delta t)e^{j2\pi\Omega_{t,1}}] \tag{32}$$

$$\begin{aligned}
R_{q,p}^{\text{SB}, \mathcal{L}}(t, f; \Delta t) \\
&= \sum_{u \in \{\text{T,R}\}} \sum_{S_i^u \in C_{\text{eff}}^{u, \mathcal{L}}} \mathbb{E}[\bar{h}_{q,p}^{S_i^u, \mathcal{L}*}(t)\bar{h}_{q,p}^{S_i^u, \mathcal{L}}(t+\Delta t)e^{j2\pi\Omega_{t,2}}]
\end{aligned} \tag{33}$$

$$\begin{aligned}
R_{q,p}^{\text{DB}, \mathcal{L}}(t, f; \Delta t) \\
&= \sum_{S_i^T \in C_{\text{eff}}^{\text{T}, \mathcal{L}}} \sum_{S_j^R \in C_{\text{eff}}^{\text{R}, \mathcal{L}}} \mathbb{E}[\bar{h}_{q,p}^{S_i, j, \mathcal{L}*}(t)\bar{h}_{q,p}^{S_i, j, \mathcal{L}}(t+\Delta t)e^{j2\pi\Omega_{t,3}}]
\end{aligned} \tag{34}$$

Second, to study the characteristics of correlation between different frequencies, the correlation function in the frequency domain is used. The revised channel transfer functions, which is frequency-dependent, of both directions have been derived in (26). Therefore, three parts of the correlation function at

different frequencies on direction \mathcal{L} can be calculated by (35)–(37), where the same time instant and the same antenna pair are required, and $\Omega_{f,1} = \Delta f \tau_{q,p}^{\text{LoS}, \mathcal{L}}(t)$, $\Omega_{f,2} = \Delta f \tau_{q,p}^{S_i^u, \mathcal{L}}(t)$, and $\Omega_{f,3} = \Delta f \tau_{q,p}^{S_i, j, \mathcal{L}}(t)$ are satisfied.

Third, to study the characteristics of correlation between antenna pairs, correlation function in the space domain is used. Three parts of the correlation function of different antenna pairs on direction \mathcal{L} can be calculated by (38)–(40), where the same time instant and the same frequency are required, and $\Omega_{l,1} = f(\tau_{q,p}^{\text{LoS}, \mathcal{L}}(t) - \tau_{q+\Delta q, p+\Delta p}^{\text{LoS}, \mathcal{L}}(t))$, $\Omega_{l,2} = f(\tau_{q,p}^{S_i^u, \mathcal{L}}(t) - \tau_{q+\Delta q, p+\Delta p}^{S_i^u, \mathcal{L}}(t))$, and $\Omega_{l,3} = f(\tau_{q,p}^{S_i, j, \mathcal{L}}(t) - \tau_{q+\Delta q, p+\Delta p}^{S_i, j, \mathcal{L}}(t))$ are satisfied.

$$R_{q,p; \Delta q, \Delta p}^{\text{LoS}, \mathcal{L}}(t, f) = \mathbb{E}[\bar{h}_{q,p}^{\text{LoS}, \mathcal{L}*}(t)\bar{h}_{q+\Delta q, p+\Delta p}^{\text{LoS}, \mathcal{L}}(t)e^{j2\pi\Omega_{l,1}}] \tag{38}$$

$$\begin{aligned}
R_{q,p; \Delta q, \Delta p}^{\text{SB}, \mathcal{L}}(t, f) \\
&= \sum_{u \in \{\text{T,R}\}} \sum_{S_i^u \in C_{\text{eff}}^{u, \mathcal{L}}} \mathbb{E}[\bar{h}_{q,p}^{S_i^u, \mathcal{L}*}(t)\bar{h}_{q+\Delta q, p+\Delta p}^{S_i^u, \mathcal{L}}(t)e^{j2\pi\Omega_{l,2}}]
\end{aligned} \tag{39}$$

$$\begin{aligned}
R_{q,p; \Delta q, \Delta p}^{\text{DB}, \mathcal{L}}(t, f) \\
&= \sum_{S_i^T \in C_{\text{eff}}^{\text{T}, \mathcal{L}}} \sum_{S_j^R \in C_{\text{eff}}^{\text{R}, \mathcal{L}}} \mathbb{E}[\bar{h}_{q,p}^{S_i, j, \mathcal{L}*}(t)\bar{h}_{q+\Delta q, p+\Delta p}^{S_i, j, \mathcal{L}}(t)e^{j2\pi\Omega_{l,3}}]
\end{aligned} \tag{40}$$

IV. RESULTS AND ANALYSES

In this section, channel statistical properties of the proposed non-reciprocal model in the THz band are simulated and analyzed. The initial distance between the BS and MS is set as $D = 70$ m. The heights of the BS and MS are 50 m and 1.5 m, respectively. The radius of the scatterer sphere at the BS side is $R_T = 40$ m and there are $N_T = 100$ scatterers on the sphere.

$$R_{q,p}^{\text{LoS},\mathcal{L}}(t, f; \Delta f) = \mathbb{E} \left[\bar{h}_{q,p}^{\text{LoS},\mathcal{L}*}(f) \left(\frac{f}{f_c} \right)^{\gamma_{\text{LoS}*}} \bar{h}_{q,p}^{\text{LoS},\mathcal{L}}(f + \Delta f) \left(\frac{f + \Delta f}{f_c} \right)^{\gamma_{\text{LoS}}} e^{j2\pi\Omega_{f,1}} \right] \quad (35)$$

$$R_{q,p}^{\text{SB},\mathcal{L}}(t, f; \Delta f) = \sum_{u \in \{\text{TR}\}} \sum_{S_i^u \in C_{\text{eff}}^{u,\mathcal{L}}} \mathbb{E} \left[\bar{h}_{q,p}^{S_i^u,\mathcal{L}*}(f) \left(\frac{f}{f_c} \right)^{\gamma_i^*} \bar{h}_{q,p}^{S_i^u,\mathcal{L}}(f + \Delta f) \left(\frac{f + \Delta f}{f_c} \right)^{\gamma_i} e^{j2\pi\Omega_{f,2}} \right] \quad (36)$$

$$R_{q,p}^{\text{DB},\mathcal{L}}(t, f; \Delta f) = \sum_{S_i^T \in C_{\text{eff}}^{T,\mathcal{L}}} \sum_{S_j^R \in C_{\text{eff}}^{R,\mathcal{L}}} \mathbb{E} \left[\bar{h}_{q,p}^{S_i^T, S_j^R,\mathcal{L}*}(f) \left(\frac{f}{f_c} \right)^{\gamma_{i,j}^*} \bar{h}_{q,p}^{S_i^T, S_j^R,\mathcal{L}}(f + \Delta f) \left(\frac{f + \Delta f}{f_c} \right)^{\gamma_{i,j}} e^{j2\pi\Omega_{f,3}} \right] \quad (37)$$

At the MS side, the radius is $R_R = 10$ m and the total number of scatterers is $N_R = 200$. When scatterers are generated in the 3D space, two sets of parameters for von Mises-Fisher distribution are used, i.e., $\kappa = 4, \theta_0 = 0, \phi_0 = -\pi/4$ for the the BS side and $\kappa = 2, \theta_0 = \pi, \phi_0 = \pi/8$ for the MS side. Moreover, with the help of HIRAN database, the molecular absorption coefficient $K_f = 0.00161 \text{ m}^{-1}$ is obtained. The configuration of antenna elements is set as the URA layout, where $P_y \times P_z = 32 \times 32$ at the BS side and $Q_y \times Q_z = 4 \times 4$ at the MS side. Three types of scatterers that exist in the urban environment are considered, i.e., building facades, trees, and concrete [52], and detailed parameters are listed in Table II. The velocity of the MS is set as $\|\mathbf{V}_{\text{MS}}\| = 1 \text{ m/s}$.

TABLE II
PARAMETERS OF SCATTERERS.

	RMS height (mm)	Index of refraction	Percentage
Building	0.05	2.5	0.6
Tree	0.08	1.3	0.2
Concrete	0.25	2.1	0.2

The scatterer generation results are shown in Fig. 7. Fig. 7(a) depicts the distribution of scatterers at BS side with $N_{\text{eff}}^{\text{T,DL}} = 31$ and $N_{\text{eff}}^{\text{T,UL}} = 56$, and Fig. 7(b) at MS side with $N_{\text{eff}}^{\text{R,DL}} = 44$ and $N_{\text{eff}}^{\text{R,UL}} = 30$. Therefore, the non-reciprocity is introduced to the modeling.

To further illustrate the properties of non-reciprocal channels, we compare the mean values of path loss and RMS delay spread between non-reciprocal channels and the traditional omnidirectional channel. The value of D is set from 50 m to 100 m, and we take a sample point every 0.1 m. The results are shown in Table III. The values of path loss and RMS delay spread of the traditional channel are both larger than the non-reciprocal channels. It can be seen that the non-reciprocal channels have better directional radiation characteristics and can maximize the use of energy, thereby improving the system efficiency.

A. Correlation between UL and DL

The correlation between DL and UL results from the reused scatterers. By examining the impact of different beamwidth on the reciprocity, the study of the correlation of non-reciprocal systems can be accomplished. The beamwidths are fixed at $[\alpha_R^{\text{DL}}, \beta_R^{\text{DL}}, \alpha_R^{\text{UL}}, \beta_R^{\text{UL}}] = [2\pi/3, \pi/4, \pi/4, \pi/4]$

TABLE III
COMPARISON OF MEAN VALUES OF CHANNEL STATISTICS BETWEEN NON-RECIPROCAL CHANNELS AND THE TRADITIONAL OMNIDIRECTIONAL CHANNEL.

	Path loss (dB)	RMS delay spread (ns)
Non-reciprocal channel (DL)	120.65	4.54
Non-reciprocal channel (UL)	121.96	8.64
Traditional channel	124.52	20.27

and $[\beta_T^{\text{DL}}, \alpha_T^{\text{UL}}, \beta_T^{\text{UL}}] = [\pi/4, \pi/4, \pi/4]$, and only the planar beamwidth for DL is changed, which is $\alpha_T^{\text{DL}} = \pi/6, \pi/3, \text{ or } \pi/2$. After 10000 Monte Carlo simulations, statistical properties of correlation between UL and DL can be obtained. The cumulative distribution functions (CDFs) of correlation coefficients of different beamwidth configurations are given in Fig. 8. As shown in the simulation result, paths of UL and DL are relevant, and the difference between beamwidths of UL and DL poses a salient impact on the correlation. The correlation coefficients get more dispersed as the beamwidth difference gets larger, indicating that the discrepancy in beamwidth reduces the correlation between UL and DL. When the UL and DL share the same antenna beam properties, channels in both directions become totally related, i.e., the conventional reciprocal systems.

B. Non-Stationarities in Time, Frequency, and Space Domains

We take DL as an example to characterize the non-stationarities of the proposed model in time, frequency, and space domains. First, the temporal autocorrelation functions (ACFs) are depicted in Fig. 9. By comparing the absolute values of local temporal ACFs at moments 0 s, 2 s, and 4 s, we can draw the conclusion that the non-stationarity in time domain is verified, which is the result of MS movement. Second, the frequency cross-correlation functions (CCFs) are shown in Fig. 10. By comparing the absolute values of frequency CCFs at different central frequencies 320 GHz, 350 GHz, and 380 GHz, the non-stationarity in frequency domain due to frequency-dependent path gain is verified. Third, the spatial CCFs are demonstrated in Fig. 11. By comparing the absolute values of spatial CCFs under three different antenna pairs, the non-stationarity in space domain due to the deployment of massive arrays is validated. The above analytical results, (29)-(33) and (36)-(38), are all compared with the simulation ones

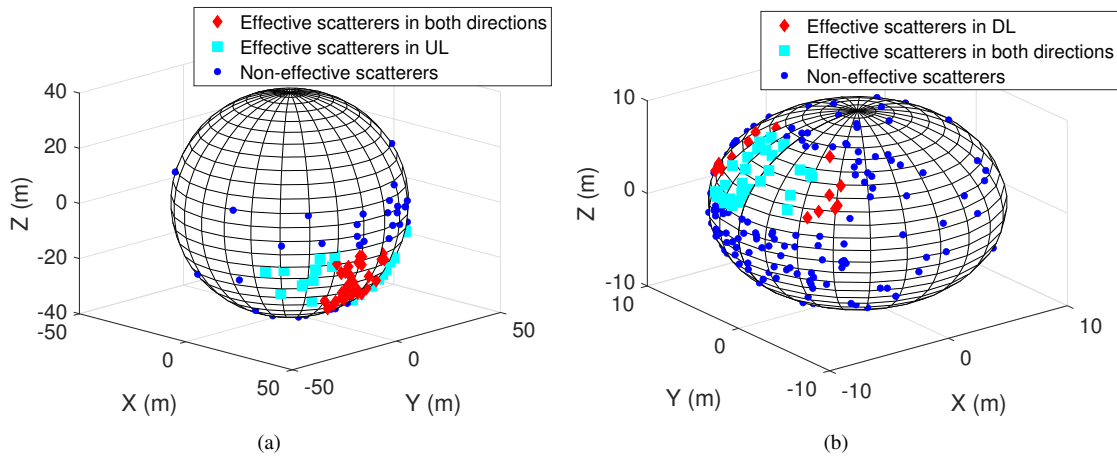


Fig. 7. Generation results of scatterers at (a) BS side and (b) MS side ($f = 350$ GHz, $D = 70$ m, $H_T = 50$ m, $H_R = 1.5$ m, $R_T = 40$ m, $N_T = 100$, $R_R = 10$ m, $N_R = 200$, $[\alpha_R^{DL}, \beta_R^{DL}, \alpha_R^{UL}, \beta_R^{UL}] = [\pi/2, \pi/4, \pi/3, \pi/4]$, $[\alpha_T^{DL}, \beta_T^{DL}, \alpha_T^{UL}, \beta_T^{UL}] = [\pi/4, \pi/4, 2\pi/3, \pi/4]$).

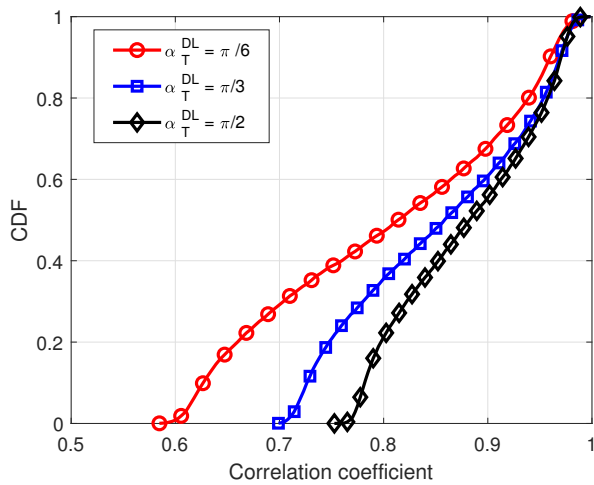


Fig. 8. CDFs of correlation coefficient between UL and DL with different planar beamwidth at the BS side in DL ($f = 350$ GHz, $D = 100$ m, $H_T = 50$ m, $H_R = 1.5$ m, $R_T = 70$ m, $N_T = 100$, $R_R = 10$ m, $N_R = 200$).

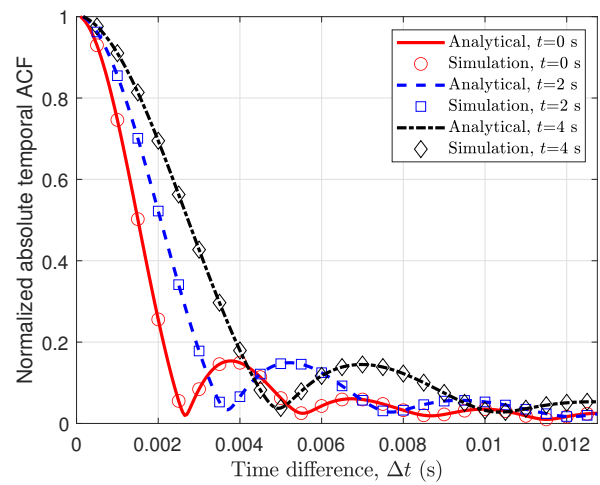


Fig. 9. Temporal ACFs at $t = 0$ s, $t = 2$ s, and $t = 4$ s ($f = 350$ GHz, $D = 70$ m, $H_T = 50$ m, $H_R = 1.5$ m, $R_T = 40$ m, $N_T = 100$, $R_R = 10$ m, $N_R = 200$, $[\alpha_R^{DL}, \beta_R^{DL}, \alpha_R^{UL}, \beta_R^{UL}] = [\pi/2, \pi/4, \pi/3, \pi/4]$, $[\alpha_T^{DL}, \beta_T^{DL}, \alpha_T^{UL}, \beta_T^{UL}] = [\pi/4, \pi/4, 2\pi/3, \pi/4]$, $\|\mathbf{V}_{MS}\| = 1$ m/s).

and good agreements are shown, which verifies the correctness of these correlation functions.

C. Scatterer Reuse and Complexity Reduction

Traditionally, channel coefficients are generated separately for both directions, which costs computation and degrades in efficiency. Since the UL and DL are correlated more or less, reusing scatterers of narrow beamwidth side when constructing the non-reciprocal scattering environment can improve the modeling efficiency.

Complexity analysis of the 3D non-reciprocal channel model takes simulation time as metric [53]. In the proposed model, scatterers are generated jointly and then classified into effective scatterers of different directions. By reusing scatterers, the responses of UL and DL can be generated simultaneously instead of independently. We use a computer with Intel Core i5 CPU and 16 GB random access memory, and results of the CIRs generation for 1000 times are given as below. The mean generation time of the proposed model

is 0.3343 ms, and for the counterpart one with independent scattering environment between UL and DL, where scatterers of both directions are generated independently, is 0.6561 ms. Therefore, the computation consumption of the proposed non-reciprocal channel model is much lower than the common one. Moreover, we define the generation of vector \mathbf{x} , which corresponds to a scatterer position, in von Mises-Fisher distribution described in Section II-B as a basic operation. When 100 scatterers on the BS sphere and 200 scatterers on the MS sphere are generated like the configurations in Section IV, we can save the calculation time of 300 basic operations for one round simulation when generating scatterers simultaneously instead of independently in DL and UL channels. Therefore, computational complexity is reduced in the proposed non-reciprocal model by reusing scatterers of the narrow beamwidth.

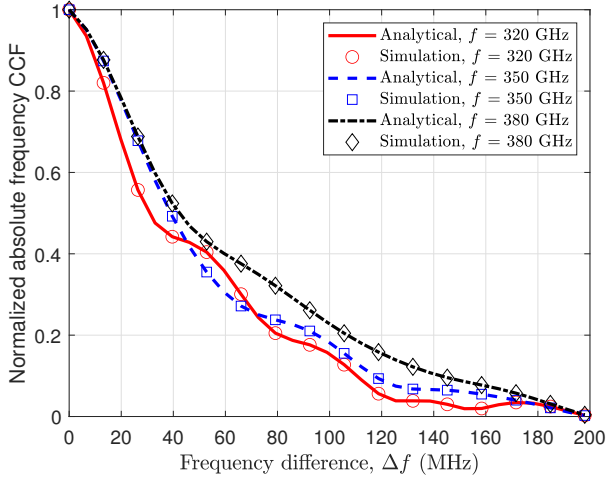


Fig. 10. Frequency CCFs at $f = 320$ GHz, $f = 350$ GHz, and $f = 380$ GHz ($D = 70$ m, $H_T = 50$ m, $H_R = 1.5$ m, $R_T = 40$ m, $N_T = 100$, $R_R = 10$ m, $N_R = 200$, $[\alpha_R^{DL}, \beta_R^{DL}, \alpha_R^{UL}, \beta_R^{UL}] = [\pi/2, \pi/4, \pi/3, \pi/4]$, $[\alpha_T^{DL}, \beta_T^{DL}, \alpha_T^{UL}, \beta_T^{UL}] = [\pi/4, \pi/4, 2\pi/3, \pi/4]$).

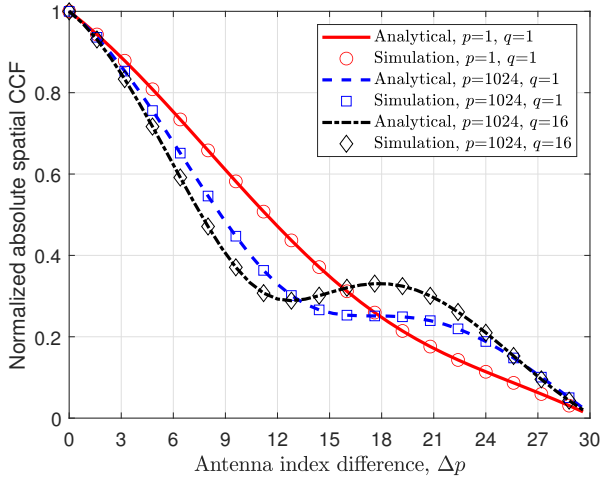


Fig. 11. Spatial CCFs of three different antenna pairs ($f = 350$ GHz, $D = 20$ m, $H_T = 10$ m, $H_R = 1.5$ m, $R_T = 10$ m, $N_T = 100$, $R_R = 3$ m, $N_R = 200$, $[\alpha_R^{DL}, \beta_R^{DL}, \alpha_R^{UL}, \beta_R^{UL}] = [\pi/2, \pi/4, \pi/3, \pi/4]$, $[\alpha_T^{DL}, \beta_T^{DL}, \alpha_T^{UL}, \beta_T^{UL}] = [\pi/4, \pi/4, 2\pi/3, \pi/4]$).

D. Model Validation

The accuracy of the channel model is crucial for link-level simulation and system performance evaluation. We compare channel statistics of the proposed model with ray-tracing ground-truth values, which are generated by the Wireless InSite software [54]. For the convenience of simulation, we adopt the configuration of a directional antenna on the BS side and an omnidirectional one on the MS side, which can be regarded as a simplification of the generalized asymmetric system [10]. The heights of the BS and MS are both set to 20 m to facilitate beam alignment. We select an urban scenario, and the surrounding environment of the BS and MS route is shown in Fig. 12. The central frequency is 350 GHz, and the beamwidth of BS in DL and UL is $[\alpha_T^{DL}, \beta_T^{DL}, \alpha_T^{UL}, \beta_T^{UL}] = [\pi/6, \pi/6, \pi/2, \pi/4]$. The transceiver distance D ranges from 50 m to 100 m and we take a sample point every 0.1 m.

The comparison of path loss at different distances between BS and MS is depicted in Fig. 13(a). It can be seen that the proposed model can well characterize the mean value and evolution trend of the path loss in UL and DL channels, except for the possible shadow fluctuations in the actual channel. In addition, the comparison of cumulative distribution function (CDF) of the RMS delay spread is shown in Fig. 13(b). The mean values of RMS delay spread and CDF curves of the proposed model and ray tracing results are similar. Therefore, the accuracy of the proposed non-reciprocal THz channel model is validated.

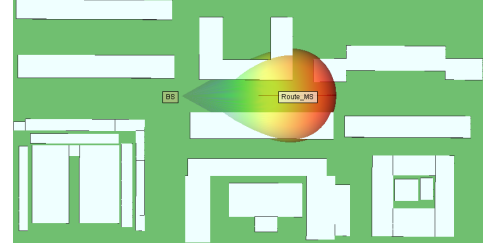


Fig. 12. Top view of urban scenario around the BS and MS route for ray tracing simulation.

V. CONCLUSIONS

In this paper, a 3D non-reciprocal and non-stationary channel model for THz asymmetric massive MIMO systems was proposed. The non-reciprocity was introduced by applying different beam patterns. Propagation features of THz bands like diffuse scattering and molecular absorption were considered in the model and verified by measured data. A DESG algorithm was designed to generate effective scatterers, and the complexity was reduced by reusing scatterers. The generation process of non-reciprocal channel was implemented in detail. The non-reciprocity and correlation between UL and DL were validated by the correlation functions. Simulation results of temporal ACFs, frequency CCFs, and spatial CCFs were compared with analytical ones, showing good agreement. The accuracy of the model was verified by comparing with the ray tracing data. Consequently, the proposed channel model could provide link-level fundamental support for 6G THz asymmetric massive MIMO systems. For future research, firstly, artificial intelligence can be used to model the relationship between beam characteristics and channel statistics; secondly, the correlation function between UL and DL channels can be utilized in the modeling process; finally, channel non-stationarity and consistency can be characterized from time, space, frequency, and beam domains.

APPENDIX A

CALCULATIONS OF ANTENNA GAIN

For simplicity, only single polarization is considered in the antenna polarization, and $G^{\mathcal{L}}(t)$ is the antenna gain, which can be expressed by

$$\sqrt{G^{\mathcal{L}}(t)} = F_T^{\mathcal{L}}(\alpha_T^{\mathcal{L}}(t), \beta_T^{\mathcal{L}}(t)) \times F_R^{\mathcal{L}}(\alpha_R^{\mathcal{L}}(t), \beta_R^{\mathcal{L}}(t)) \quad (41)$$

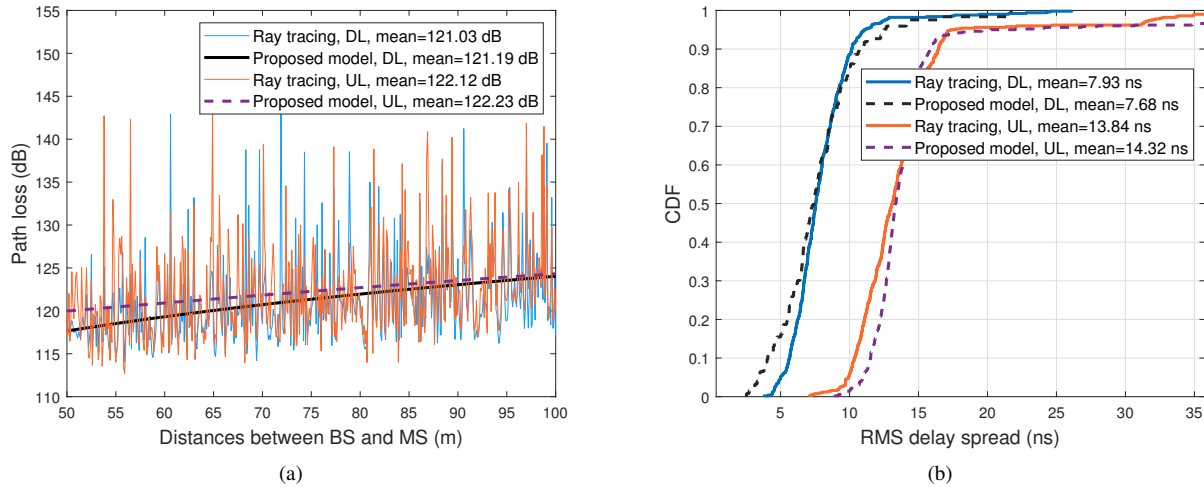


Fig. 13. Comparison of the proposed model with ray tracing. (a) Variation of path loss with distance between the BS and MS; and (b) CDF curves of the RMS delay spread.

where $F_u^{\mathcal{L}}(\alpha_T^{\mathcal{L}}(t), \beta_T^{\mathcal{L}}(t))$ represents the antenna gain of u side for direction \mathcal{L} with the beamwidth of planar and vertical angles, α and β , respectively.

The effective scatterer surface area E_A can be given by [55]

$$S_{E_A} = 4R^2 \arcsin\left(\tan \frac{\alpha}{2} \tan \frac{\beta}{2}\right). \quad (42)$$

It is assumed that the planar and vertical angles remain constant during the generation process of channel coefficients. Therefore, the antenna gain $F_u^{\mathcal{L}}(\alpha_T^{\mathcal{L}}(t), \beta_T^{\mathcal{L}}(t))$ of one side for a certain direction can be calculated as

$$\begin{aligned} F(\alpha, \beta) &= \frac{S_{\text{Sphere}}}{S_{E_A}} = \frac{4\pi R^2}{4R^2 \arcsin\left(\tan \frac{\alpha}{2} \tan \frac{\beta}{2}\right)} \\ &= \frac{\pi}{\arcsin\left(\tan \frac{\alpha}{2} \tan \frac{\beta}{2}\right)}. \end{aligned} \quad (43)$$

In other words, we use planar and vertical beamwidth to calculate the antenna gain, which is applicable to array gain of arbitrary beam shape.

APPENDIX B

CALCULATIONS OF ATTENUATIONS DUE TO FREE-SPACE PROPAGATION AND MOLECULAR ABSORPTION

Attenuation due to free-space propagation can be calculated as follows according to the Fries formula

$$A_{\text{prop}} = \left(\frac{c}{4\pi f d}\right)^2. \quad (44)$$

In (44), c is the speed of light, f is the frequency of signal, and d is the distance that ray travels. Attenuation due to molecular absorption is crucial in THz bands. It is determined by the composition of air, temperature, pressure of the propagation environment, and the frequency of signal. Attenuation due to molecular absorption is given by

$$A_{\text{ma}} = e^{-K_f d} \quad (45)$$

where K_f denotes the absorption coefficient, which is mainly influenced by the composition of air and varies along with frequency f . With the help of the online simulation website HITRAN [56], the molecular absorption coefficient K_f under different propagation environments can be obtained.

Total attenuation due to free-space propagation and molecular absorption in the THz band can be calculated by

$$A_{\text{total}} = A_{\text{ma}} \cdot A_{\text{prop}}. \quad (46)$$

A_{total} in dB can be written as

$$\begin{aligned} A_{\text{total}}[\text{dB}] &= 10 \log_{10}(A_{\text{total}}) \\ &= 147.56 - 20 \log_{10}(f d) - 4.34 K_f d [\text{dB}]. \end{aligned} \quad (47)$$

REFERENCES

- [1] C.-X. Wang *et al.*, "On the road to 6G: Visions, requirements, key technologies and testbeds," *IEEE Commun. Surveys Tuts.*, vol. 25, no. 2, pp. 905–974, 2023.
- [2] X. Cheng, Z. Huang, and L. Bai, "Channel nonstationarity and consistency for beyond 5G and 6G: A survey," *IEEE Commun. Surveys Tuts.*, vol. 24, no. 3, pp. 1634–1669, 2022.
- [3] Z. Wei, F. Liu, C. Masouros, N. Su, and A. P. Petropulu, "Toward multifunctional 6G wireless networks: Integrating sensing, communication, and security," *IEEE Commun. Mag.*, vol. 60, no. 4, pp. 65–71, Apr. 2022.
- [4] Z. Chen *et al.*, "Terahertz wireless communications for 2030 and beyond: A cutting-edge frontier," *IEEE Commun. Mag.*, vol. 59, no. 11, pp. 66–72, Nov. 2021.
- [5] C.-X. Wang *et al.*, "6G wireless channel measurements and models: Trends and challenges," *IEEE Veh. Technol. Mag.*, vol. 15, no. 4, pp. 22–32, Dec. 2020.
- [6] T. Zhou, Y. Yang, L. Liu, C. Tao, and Y. Liang, "A dynamic 3-D wideband GBSM for cooperative massive MIMO channels in intelligent high-speed railway communication systems," *IEEE Trans. Wireless Commun.*, vol. 20, no. 4, pp. 2237–2250, Apr. 2021.
- [7] J. Morte Palacios, O. Raeesi, A. Gokceoglu, and M. Valkama, "Impact of channel non-reciprocity in cell-free massive MIMO," *IEEE Wireless Commun. Lett.*, vol. 9, no. 3, pp. 344–348, Mar. 2020.
- [8] W. Hong *et al.*, "The role of millimeter-wave technologies in 5G/6G wireless communications," *IEEE J. Microw.*, vol. 1, no. 1, pp. 101–122, Jan. 2021.
- [9] W. Hong *et al.*, "Asymmetric full-digital beamforming mmWave massive MIMO systems for B5G/6G wireless communications," in *Proc. IEEE Asia-Pacific Microw. Conf. (APMC)*, 2020, pp. 31–32.

- 1
2
3
4
5
6
7
8
9
10
11
12
13
14
15
16
17
18
19
20
21
22
23
24
25
26
27
28
29
30
31
32
33
34
35
36
37
38
39
40
41
42
43
44
45
46
47
48
49
50
51
52
53
54
55
56
57
58
59
60
- [10] C. Guo *et al.*, "Design and implementation of a full-digital beamforming array with nonreciprocal Tx/Rx beam patterns," *IEEE Antennas Wireless Propag. Lett.*, vol. 19, no. 11, pp. 1978–1982, Nov. 2020.
- [11] B. De Beelde, E. Tanghe, M. Yusuf, D. Plets, and W. Joseph, "Radio channel modeling in a ship hull: Path loss at 868 MHz and 2.4, 5.25, and 60 GHz," *IEEE Antennas Wireless Propag. Lett.*, vol. 20, no. 4, pp. 597–601, Apr. 2021.
- [12] M.-D. Kim, J. Liang, J. Lee, J. Park, and B. Park, "Directional multipath propagation characteristics based on 28 GHz outdoor channel measurements," in *Proc. 10th Eur. Conf. Antennas Propag. (EuCAP)*, 2016, pp. 1–5.
- [13] J. Lee *et al.*, "Directional delay spread characteristics of outdoor-to-indoor propagation based on millimeter-wave measurements," in *Proc. 13th Eur. Conf. Antennas Propag. (EuCAP)*, 2019, pp. 1–5.
- [14] M. K. Samimi and T. S. Rappaport, "Statistical channel model with multi-frequency and arbitrary antenna beamwidth for millimeter-wave outdoor communications," in *Proc. IEEE Globecom Workshops (GC Wkshps)*, 2015, pp. 1–7.
- [15] J. Zhang, L. Liu, Z. Tan, and K. Wang, "A semi-deterministic MIMO-based beam channel model of ray-tracing and propagation-graph for mmwave communications," in *Proc. IEEE Inter. Conf. Commun. Workshops (ICC Wkshps)*, 2022, pp. 1135–1140.
- [16] J. Zhang, L. Liu, Z. Tan, K. Wang, and T. Zhou, "Analysis of joint angular distribution for nonreciprocal beams via the mixture of Gaussian distribution based on ray-tracing," *Inter. J. Antennas Propag.*, vol. 2022, no. 3505181, 2022.
- [17] J. Zhang, L. Liu, Z. Tan, T. Zhou, and K. Wang, "Analysis of asymmetric beam channel characteristics based on 3D geometric channel model," *J. Beijing University Posts Telecommunications*, vol. 45, no. 2, pp. 98–103, 2022.
- [18] F. Lai, C.-X. Wang, J. Huang, X. Gao, and F.-C. Zheng, "A novel beam domain channel model for B5G massive MIMO wireless communication systems," *IEEE Trans. Veh. Technol.*, vol. 72, no. 4, pp. 4143–4156, Apr. 2023.
- [19] J. Bian *et al.*, "A novel 3D beam domain channel model for massive MIMO communication systems," *IEEE Trans. Wireless Commun.*, vol. 22, no. 3, pp. 1618–1632, Mar. 2023.
- [20] H. Chang *et al.*, "A novel 3D beam domain channel model for UAV massive MIMO communications," *IEEE Trans. Wireless Commun.*, early access, 2023, doi: 10.1109/TWC.2023.3233961.
- [21] Z. He *et al.*, "Ensemble-transfer-learning-based channel parameter prediction in asymmetric massive MIMO systems," *Frontiers Inf. Technol. Electron. Eng.*, vol. 24, no. 2, pp. 275–288, 2023.
- [22] M. Yuan, W. Zhang, K. Zhang, and Y. Zhang, "Channel attention-based path loss prediction model in asymmetric massive MIMO systems," in *Proc. IEEE Global Commun. Conf. (GLOBECOM)*, 2022, pp. 723–728.
- [23] K. Guan, H. Yi, D. He, B. Ai, and Z. Zhong, "Towards 6G: Paradigm of realistic terahertz channel modeling," *China Commun.*, vol. 18, no. 5, pp. 1–18, May 2021.
- [24] P. Xie *et al.*, "Terahertz wave propagation characteristics on rough surfaces based on full-wave simulations," *Radio Sci.*, vol. 57, no. 6, pp. 1–16, Jun. 2022.
- [25] D. Serghiou, M. Khalily, T. W. C. Brown, and R. Tafazolli, "Terahertz channel propagation phenomena, measurement techniques and modeling for 6G wireless communication applications: A survey, open challenges and future research directions," *IEEE Commun. Surveys Tuts.*, vol. 24, no. 4, pp. 1957–1996, 2022.
- [26] Y. Chen, R. Li, C. Han, S. Sun, and M. Tao, "Hybrid spherical- and planar-wave channel modeling and estimation for terahertz integrated UM-MIMO and IRS systems," *IEEE Trans. Wireless Commun.*, early access, 2023, doi: 10.1109/TWC.2023.3273221.
- [27] H. Cho, B. Ko, B. Clerckx, and J. Choi, "Coverage increase at THz frequencies: A cooperative rate-splitting approach," *IEEE Trans. Wireless Commun.*, early access, 2023, doi: 10.1109/TWC.2023.3273720.
- [28] K. Guan *et al.*, "5G channel models for railway use cases at mmWave band and the path towards terahertz," *IEEE Intell. Transp. Syst. Mag.*, vol. 13, no. 3, pp. 146–155, 2021.
- [29] J. Gomez-Ponce, N. A. Abbasi, A. E. Willner, C. J. Zhang, and A. F. Molisch, "Directionally resolved measurement and modeling of THz band propagation channels," *IEEE Open J. Antennas Propag.*, vol. 3, pp. 663–686, Jun. 2022.
- [30] S. Ju, Y. Xing, O. Kanher, and T. S. Rappaport, "Millimeter wave and sub-terahertz spatial statistical channel model for an indoor office building," *IEEE J. Sel. Areas Commun.*, vol. 39, no. 6, pp. 1561–1575, Jun. 2021.
- [31] N. A. Abbasi *et al.*, "Double-directional channel measurements for urban THz communications on a linear route," in *Proc. IEEE Int. Conf. Commun. Workshops (ICC Wkshps)*, 2021, pp. 1–6.
- [32] P. Tang *et al.*, "Channel measurement and path loss modeling from 220 GHz to 330 GHz for 6G wireless communications," *China Commun.*, vol. 18, no. 5, pp. 19–32, May 2021.
- [33] H. Yi *et al.*, "Characterization for the vehicle-to-infrastructure channel in urban and highway scenarios at the terahertz band," *IEEE Access*, vol. 7, pp. 166984–166996, 2019.
- [34] J. Wang, C.-X. Wang, J. Huang, and Y. Chen, "6G THz propagation channel characteristics and modeling: Recent developments and future challenges," *IEEE Commun. Mag.*, early access, 2022, doi: 10.1109/MCOM.001.2200403.
- [35] C.-X. Wang *et al.*, "Key technologies in 6G terahertz wireless communication systems: A survey," *IEEE Veh. Technol. Mag.*, vol. 16, no. 4, pp. 27–37, 2021.
- [36] J. Wang *et al.*, "A novel 3D non-stationary GBSM for 6G THz ultra-massive MIMO wireless systems," *IEEE Trans. Veh. Technol.*, vol. 70, no. 12, pp. 12312–12324, Dec. 2021.
- [37] Y. Zhang, L. Zhao, and Z. He, "A 3-D hybrid dynamic channel model for indoor THz communications," *China Commun.*, vol. 18, no. 5, pp. 50–65, May 2021.
- [38] J. Wang, C.-X. Wang, J. Huang, H. Wang, and X. Gao, "A general 3D space-time-frequency non-stationary THz channel model for 6G ultra-massive MIMO wireless communication systems," *IEEE J. Sel. Areas Commun.*, vol. 39, no. 6, pp. 1576–1589, Jun. 2021.
- [39] Y. Yuan *et al.*, "A 3D geometry-based THz channel model for 6G ultra massive MIMO systems," *IEEE Trans. Veh. Technol.*, vol. 71, no. 3, pp. 2251–2266, Mar. 2022.
- [40] J. Bian, C.-X. Wang, X. Gao, X. You, and M. Zhang, "A general 3D non-stationary wireless channel model for 5G and beyond," *IEEE Trans. Wireless Commun.*, vol. 20, no. 5, pp. 3211–3224, May 2021.
- [41] A. Shafie *et al.*, "Coverage analysis for 3D terahertz communication systems," *IEEE J. Sel. Areas Commun.*, vol. 39, no. 6, pp. 1817–1832, Jun. 2021.
- [42] K. Mammassis, P. Santi, and A. Goulianos, "A three-dimensional angular scattering response including path powers," *IEEE Trans. Wireless Commun.*, vol. 11, no. 4, pp. 1321–1333, Apr. 2012.
- [43] G. S. Watson, "Distributions on the circle and sphere," *J. Appl. Probability*, vol. 19, no. A, pp. 265–280, 1982.
- [44] K. Guan *et al.*, "Channel characterization and capacity analysis for THz communication enabled smart rail mobility," *IEEE Trans. Veh. Technol.*, vol. 70, no. 5, pp. 4065–4080, May 2021.
- [45] F. Sheikh, Y. Gao, and T. Kaiser, "A study of diffuse scattering in massive MIMO channels at terahertz frequencies," *IEEE Trans. Antennas Propag.*, vol. 68, no. 2, pp. 997–1008, Feb. 2020.
- [46] D. He *et al.*, "Stochastic channel modeling for kiosk applications in the terahertz band," *IEEE Trans. THz Sci. Technol.*, vol. 7, no. 5, pp. 502–513, Sep. 2017.
- [47] G. A. Siles, J. M. Riera, and P. Garcia-del Pino, "Atmospheric attenuation in wireless communication systems at millimeter and THz frequencies [wireless corner]," *IEEE Trans. Antennas Propag.*, vol. 57, no. 1, pp. 48–61, Feb. 2015.
- [48] C. Jansen *et al.*, "Diffuse scattering from rough surfaces in THz communication channels," *IEEE Trans. THz Sci. Technol.*, vol. 1, no. 2, pp. 462–472, Nov. 2011.
- [49] Y. Tan, C.-X. Wang, J. O. Nielsen, G. F. Pedersen, and Q. Zhu, "A novel B5G frequency nonstationary wireless channel model," *IEEE Trans. Antennas Propag.*, vol. 69, no. 8, pp. 4846–4860, Aug. 2021.
- [50] J. Huang, C.-X. Wang, H. Chang, J. Sun, and X. Gao, "Multi-frequency multi-scenario millimeter wave MIMO channel measurements and modeling for B5G wireless communication systems," *IEEE J. Sel. Areas Commun.*, vol. 38, no. 9, pp. 2010–2025, Sep. 2020.
- [51] C.-X. Wang *et al.*, "Pervasive wireless channel modeling theory and applications to 6G GBSMs for all frequency bands and all scenarios," *IEEE Trans. Veh. Technol.*, vol. 71, no. 9, pp. 9159–9173, Sep. 2022.
- [52] R. Piesiewicz *et al.*, "Terahertz characterisation of building materials," *Electron. Lett.*, vol. 41, no. 18, pp. 1002–1004, 2005.
- [53] Y. Zhang *et al.*, "Accuracy-complexity tradeoff analysis and complexity reduction methods for non-stationary IMT-A MIMO channel models," *IEEE Access*, vol. 7, pp. 178047–178062, 2019.
- [54] Remcom. Wireless insite. [Online]. Available: <https://www.remcom.com/wireless-insite-em-propagation-software>
- [55] R. Kovalchukov *et al.*, "Evaluating SIR in 3D millimeter-wave deployments: Direct modeling and feasible approximations," *IEEE Trans. Wireless Commun.*, vol. 18, no. 2, pp. 879–896, Feb. 2019.
- [56] HITRAN. Hitran website. [Online]. Available: <https://hitran.iao.ru/home>

Responses to Reviewers' Comments

(Manuscript Number: Paper-TW-Mar-23-0388)

A Non-Reciprocal Channel Model for THz Asymmetric Massive MIMO Systems

Kaien Zhang, Yan Zhang, Cheng-Xiang Wang, Xiping Wu, and Chuan Du

Dear Dr. Ljiljana Simic,

On behalf of my co-authors, we would like to thank you and all the Reviewers for the valuable reviews and we are grateful for this opportunity to revise our manuscript. We appreciate the time and efforts spent in reviewing this paper and providing constructive comments. We have carefully revised our manuscript based on all the Reviewers' suggestions. All revisions are highlighted in blue color in this revised version, and we believe that our revisions and following responses have addressed all concerns raised. Detailed responses to the Reviewers' comments are provided as follows.

Yours Sincerely,

Cheng-Xiang Wang and Yan Zhang

Response to Reviewer 1's Comments

Comment 1.1:

The explanation is unclear, especially related to how scattering is added in the modeling (essential for THz modeling).

Response:

The way in which scattering is added to the THz modeling process is explained in detail as follows, and we have added the explanations in the revised manuscript.

First, we initialize the parameters of the materials involved in propagation. We set the RMS height $\rho_{h,c}$, index of refraction $n_{t,c}$, and the probability of occurrence P_c for each material in the propagation scenario. For the urban scenario in the paper, we take three typical kinds of materials into account, i.e., building, tree, and concrete, and the specific values of $\rho_{h,c}$, $n_{t,c}$, and P_c are given in Table II in the paper.

Second, we determine whether reflection or diffuse scattering occurs at each point. For each scatterer position generated by the directive effective scatterer generation algorithm, the material type of the position is obtained according to P_c . After that, we randomly generate the orientation of the rough surface and use the relationship between the incident angle and the outgoing angle to judge whether the path is reflection or scattering.

Third, we multiply the attenuation factor in the channel impulse response. We calculate the reflection coefficient χ_{ref} or the scattering coefficient χ_{sca} for each position, according to Eq. (8)-(10). Then in the channel impulse response formula, we multiply the single-bounce attenuation coefficient χ^{SB} and double-bounce attenuation coefficient χ^{DB} by the total gain as shown in Eq. (17) and Eq. (21).

In the sixth paragraph of Section II-D on page 6, we have explained clearly how scattering is added in the modeling as follows: “[In the modeling process, each effective scatterer position is assigned a kind of material according to \$P_c\$. Then, the orientation of the rough surface in each position is randomly generated, and each ray is classified as either scattered or reflected by its angles. At last, the attenuation coefficient is calculated and multiplied in the channel impulse response.](#)”.

Comment 1.2:

The difference between this work and other GBSCM models is stated in the introduction. However, I would encourage the authors to demonstrate the improvements of this model versus previously proved GBSCM models in THz; because, at first sight, there is no significant difference between the author's model and previous GBSCM; or at least it is not clearly shown.

Response:

We elaborate on the improvements from three aspects. Detailed explanations are as follows, and we have clearly shown these improvements in the revised manuscript.

(1) We fill the research gap in non-reciprocal channel modeling.

The existing THz GBSCMs cannot be applied to the asymmetric massive MIMO systems, like in [A], [5], and [36-40], because they cannot establish and utilize the relationship between DL and UL channels. In addition, the existing THz GBSCMs are based on the assumption of twin clusters. The positions and parameters of clusters and

rays are randomly generated in each simulation, and the spatial consistency after coupling with the beam domain cannot be guaranteed. Due to those problems and the excellent performance of asymmetric massive MIMO systems, channel modeling under this configuration is very meaningful but challenging work.

[A] L. Bai, Z. Huang, X. Zhang, and X. Cheng, "A non-stationary 3D model for 6G massive MIMO mmWave UAV channels," *IEEE Trans. Wireless Commun.*, vol. 21, no. 6, pp. 4325-4339, Jun. 2022.

Our research for the first time fills this research gap. We propose the beam model and the concept of effective scatterers (including the generation algorithm). By using the correlation of DL and UL channels, the model can simultaneously generate bidirectional channels, and it also has spatial consistency while reducing complexity. At the same time, we for the first time give the analytical formula and simulation results of the correlation function of the DL and UL channels. The above research results are not involved in the existing THz channel modeling research.

(2) We design the THz propagation characteristics closer to actual channels.

In the existing THz channel modeling work, there is no complete molecular absorption and diffuse scattering model for each ray suitable for urban scenarios.

In [36], the authors modeled the THz channels in terms of clusters and assumed that the center of the cluster was a specular path. In [37], molecular absorption and diffuse scattering were considered, which were only applied to the indoor scenario. In [38], only the molecular absorption was modeled. In [39], the molecular absorption and diffuse scattering were not taken into account. In [40], the oxygen molecules absorption loss was considered, but the absorption loss of water molecules was not considered, which is also very important in the THz band.

We design the molecular absorption and diffuse scattering model for the urban THz scenario and give detailed implementation steps. By comparing with the measured data in Fig. 5, we verify that the proposed model can accurately characterize the THz attenuation characteristics.

Moreover, the ultra-large bandwidth of the THz frequency band makes the multipath resolution extremely high, and the multipath clustering phenomenon is weak, which is proven by THz channel measurements [B, C]. Thus, the THz attenuation model we have designed acts on each ray separately, which is more suitable for the high-resolution characteristics of the THz frequency band.

[B] F. Undi, A. Schultze, W. Keusgen, M. Peter, and T. Eichler, "Angle-resolved THz channel measurements at 300 GHz in an outdoor environment," in *Proc. IEEE Inter. Conf. Commun. Workshops (ICC Wkshps)*, 2021, pp. 1-7.

[C] M. Schmieder *et al.*, "THz channel sounding: Design and validation of a high performance channel sounder at 300 GHz," in *Proc. IEEE Wireless Commun. Networking Conf. Workshops (WCNCW)*, 2020, pp. 1-6.

(3) We modify the double-sphere geometric model to support the large bandwidth.

Due to the large bandwidth of the THz frequency band, the THz channel model needs to provide high delay resolution. However, the existing double-sphere model like [39] cannot be applied to broadband channels, because the two spheres are directly connected, resulting in low delay resolution. We modify the double-sphere model by adding virtual links between the two spheres, making the model usable for THz

wideband systems.

In addition, the reason for adopting the double-sphere model is this method is more suitable for THz asymmetric systems. The conventional twin-cluster stochastic model in [A], [36-38], and [40] makes it difficult to couple the beam domain, and it cannot establish and utilize the relationship between DL and UL channels and generate bidirectional channel responses at the same time. Meanwhile, the twin-cluster model is not effective for short-distance spatial consistency. The double-sphere model can just solve the above problems.

In the seventh paragraph of the Introduction on page 2, we have briefly illustrated the improvements as follows: “Compared with the existing models, there are three aspects of improvement. First, we establish and utilize the relationship between DL and UL channels and generate correlated bidirectional channel responses simultaneously, thus reducing complexity and maintaining spatial consistency. Second, the molecular absorption and diffuse scattering are considered for each ray to fit THz propagation properties. Third, we improve the double-sphere model by adding virtual links to meet the requirement of large bandwidth.”.

Comment 1.3:

The authors should also explain better how they include the near-field behavior of the antennas when the scatterers are in the near-field region. Antenna patterns are not the same in the near and far fields.

Response:

We have deleted the discussions about the spherical wave and the near-field effect in the paper because they do not exist in the proposed channel model.

The Rayleigh distance is calculated as

$$D_R = \frac{2L^2}{\lambda} = \frac{2\left(\sqrt{2}(N-1) \cdot \frac{\lambda}{2}\right)^2}{\lambda} = (N-1)\lambda = (N-1)\frac{c}{f_c} .$$

L is the antenna array

aperture, which is the length of the diagonal of the $N \times N$ UPA, λ is the wavelength, c is the speed of light, and f_c is the central frequency. Under the simulation parameter configurations in this paper, the BS side is a 32×32 UPA, the MS side is a 4×4 UPA, and the center frequency is 350 GHz. Therefore, the Rayleigh distance at the BS side is 0.8237 m, and at the MS side is 0.0077 m. The Rayleigh distances on both sides are much smaller than the radius of the scatterer spheres (40 m at BS and 10 m at MS), so it can be assumed that the scatterers are in the far field of the antenna.

Comment 1.4:

On page 16, line 24, and page 17, line 15 (or 16), the authors show a formula to compute the distance a ray travels from the transmitter to the receiver. However, I notice they multiply the distance by the scattering attenuation factor. I wonder why a value in meters has to be multiplied by a ratio of powers (e.g., attenuation). Traveled distance impacts attenuation, but this implies that scattering attenuation impacts the traveled

1
2
3 *distance of a ray. Could you please explain this effect and provide references as well?*

4
5 **Response:**

6 We apologize for the misunderstanding caused by not writing clearly. In fact, the
7 symbol before χ is a period instead of a multiplication sign, which leads to
8 misunderstanding. We have modified the word order of the sentences in the revised
9 version.
10

11
12
13 **Comment 1.5:**

14 *A comparison against Ray tracer or measurements (if possible) could provide a*
15 *good assessment of the accuracy of this model.*

16
17 **Response:**

18 We have added the comparison against the ray tracer to provide a good assessment
19 of the accuracy of this model. The simulated urban scenario is shown in Fig. 12, and
20 the comparison results of channel statistics (path loss and RMS delay spread) are
21 depicted in Fig. 13(a) and (b). The results show that the statistics of the proposed model
22 are in good agreement with the simulation ones, and can accurately represent the actual
23 channel characteristics.
24

25 In Section IV-D on page 12, we have added the comparison with ray tracing as
26 follows: “The accuracy of the channel model is crucial for link-level simulation and
27 system performance evaluation. We compare channel statistics of the proposed model
28 with ray-tracing ground-truth values, which are generated by the Wireless InSite
29 software [54]. For the convenience of simulation, we adopt the configuration of a
30 directional antenna on the BS side and an omnidirectional one on the MS side, which
31 can be regarded as a simplification of the generalized asymmetric system [10]. The
32 heights of the BS and MS are both set to 20 m to facilitate beam alignment. We select
33 an urban scenario, and the surrounding environment of the BS and MS route is shown
34 in Fig. 12. The central frequency is 350 GHz, and the beamwidth of BS in DL and UL
35 is $[\alpha_T^{DL}, \beta_T^{DL}, \alpha_T^{UL}, \beta_T^{UL}] = [\pi/6, \pi/6, \pi/2, \pi/4]$. The transceiver distance D ranges
36 from 50 m to 100 m and we take a sample point every 0.1 m.
37

38 The comparison of path loss at different distances between BS and MS is depicted
39 in Fig. 13(a). It can be seen that the proposed model can well characterize the mean
40 value and evolution trend of the path loss in UL and DL channels, except for the
41 possible shadow fluctuations in the actual channel. In addition, the comparison of
42 cumulative distribution function (CDF) of the RMS delay spread is shown in Fig. 13(b).
43 The mean values of RMS delay spread and CDF curves of the proposed model and ray
44 tracing results are similar. Therefore, the accuracy of the proposed non-reciprocal THz
45 channel model is validated.”.
46
47
48
49
50

51
52
53 **Response to Reviewer 2’s Comments**

54
55 **Comment 2.1:**

56 *In the Introduction, the authors introduced the advantages of the THz band to meet*
57 *the requirement of the asymmetric massive MIMO systems. Some highly related*
58 *references should also be cited.*
59
60

Response:

According to the reviewer's suggestion, we additionally cite the three most relevant papers on THz channels in the sixth paragraph of the Introduction on page 2. The added references are as follows:

[25] D. Serghiou, M. Khalily, T. W. C. Brown, and R. Tafazolli, "Terahertz channel propagation phenomena, measurement techniques and modeling for 6G wireless communication applications: A survey, open challenges and future research directions," *IEEE Commun. Surveys Tuts.*, vol. 24, no. 4, pp. 1957-1996, 2022.

[26] Y. Chen, R. Li, C. Han, S. Sun, and M. Tao, "Hybrid spherical- and planar-wave channel modeling and estimation for terahertz integrated UM-MIMO and IRS systems," *IEEE Trans. Wireless Commun.*, early access, 2023, doi: 10.1109/TWC.2023.3273221.

[27] H. Cho, B. Ko, B. Clerckx, and J. Choi, "Coverage increase at THz frequencies: A cooperative rate-splitting approach," *IEEE Trans. Wireless Commun.*, early access, 2023, doi: 10.1109/TWC.2023.3273720.

Comment 2.2:

The structure of Section II should be reorganized to be clear enough. For example, the modeling of antenna beams and the DESG algorithm should be divided into two parts. The spherical-wave model should be a separate part, instead of mixing in CIRs generating, and the corresponding simulation result (Fig. 8) can be presented here.

Response:

We have modified the structure of Section II according to the reviewer's advice to make it clear enough. In addition, the part of the spherical-wave model is deleted according to the response of comment 1.3.

Comment 2.3:

The asymmetry of the channel model should be highlighted in the result analysis section. For example, the authors should provide the generation results of scatterers in the uplink and downlink channels of beam asymmetric systems, in order to clearly demonstrate the non-reciprocity of the propagation environment (both uplink and downlink for BS and UE sides).

Response:

We have added the scatterer generation results of both UL and DL at the BS and UE sides in Fig. 7. We use different colors to distinguish effective scatterers and invalid scatterers, as well as common scatterers for UL and DL. Through this visualization result, the beam asymmetry of the proposed model is clearly displayed.

At the same time, please note that the spherical surface of the scatterer on the MS side is also a true sphere, not an ellipsoid, and it is just a reason for adjusting the viewing angle for clear observation. In Section IV on page 10, we have given the scatterer generation results as follows: "The scatterer generation results are shown in Fig. 7. Fig. 7(a) depicts the distribution of scatterers at BS side with $N_{eff}^{T,DL} = 31$ and $N_{eff}^{T,UL} = 56$, and Fig. 7(b) at MS side with $N_{eff}^{R,DL} = 44$ and $N_{eff}^{R,UL} = 30$. Therefore, the non-reciprocity is introduced to the modeling."

Comment 2.4:

Some figures are unclear or have incorrect formatting, e.g., (1) In Fig. 2, the annotation of angles and scattering points is not clear enough, and some line segments overlap together. (2) Fig. 2 and Fig. 3 both represent the geometric relationships of the model, considering merging them into one figure. (3) The variables in the coordinate axis should be in italics, for example, Fig. 8, Fig. 10, Fig. 11, and Fig. 12. Check all the figures carefully. (4) Some figures have boxes, e.g., Fig. 6 and Fig. 9, while others do not, e.g., Fig. 10-12.

Response:

We have carefully revised the figures that are mentioned by the reviewer. Specifically, we have modified the annotation of angles, the scattering points, and the line segments to make it clear enough, and we have merged Fig. 2 and Fig. 3 considering they both represent geometric relationships. We have modified the format of variables in the figures. At last, we have added boxes to the figures.

Comment 2.5:

In Eq. (11), the channel impulse response is expressed as the sum of the LoS part and NLoS part. But the attenuation of the signal has already been calculated by the free space loss as Eq. (42) and molecular absorption loss as Eq. (33) in Appendix B, why multiply again the distribution coefficient of the Rician K factor? Check this matter and modify the relevant formulas and deductions.

Response:

We have discussed this issue carefully, and the Rician K factor really should not appear in the formula of the channel model. Since we calculate the signal amplitude jointly by free space loss, molecular absorption loss, and diffuse scattering loss, there is no need to multiply the Rician K factor. We have revised all the formula derivations involved (Eq. 11, Eq. 24-28, and Eq. 30-38).

Comment 2.6:

As this article is a pioneering work in channel modeling for asymmetric MIMO systems, it is best for the author to include future trends in this research direction, such as how to more accurately represent the relationship between asymmetric beams, channel parameters, and propagation environment, how to utilize the correlation between uplink and downlink channels, and how to characterize the non-stationarity and consistency in asymmetric massive MIMO systems, etc., in order to provide guidance for future research.

Response:

We elaborate on the trends from three perspectives, corresponding to the three points the reviewer says, and we have briefly illustrated the future trends in the Conclusions.

(1) For an asymmetric system modeled in the beam domain, different beamwidth will filter different combinations of visible scatterers, resulting in changes in the statistical characteristics of the channel. Therefore, there is a certain mapping relationship between the beamwidth and the large-scale parameters. In the future,

artificial intelligence-related algorithms can be used to model this relationship to achieve more accurate beam domain modeling. In addition, certain parameter fluctuations will also occur at the edge and center of the same beam, which can be solved by combining in-depth research on the array radiation mechanism and artificial intelligence.

(2) For the correlation of the UL and DL channels, we have derived the formula of the correlation function in the paper and analyzed the influence of the beamwidth on it. If we want to use this correlation in the future, referring to the method of dealing with different links in the standardized channel model, we can add correlation to the large-scale parameters of the DL and UL channels determined by the beam characteristics to more accurately model the asymmetric characteristics.

(3) For the characterization of non-stationary and consistency in beam asymmetric systems, the model in this paper can already meet the basic needs. For future research, those two key channel characteristics can be extended to multiple domains (space domain, time domain, frequency domain, and beam domain), and explore the non-stationarity of parameters and the birth-death process of multipath in multiple domains. The continuous change of various characteristics, i.e., the channel consistency, can also be studied in those domains.

In the Conclusions, we have added the future trends as “For future research, firstly, artificial intelligence can be used to model the relationship between beam characteristics and channel statistics; secondly, the correlation function between UL and DL channels can be utilized in the modeling process; finally, channel non-stationarity and consistency can be characterized from time, space, frequency, and beam domains.”.

Comment 2.7:

There are still some typos or mistakes in the manuscript, and I list some of them. Please check carefully throughout the paper. (1) The literature research in the Introduction should use the simple past tense. (2) In Section IV-A, the beamwidth is expressed like $\{X, Y, Z \dots\} = \{x1, y1, z1 \dots\}$, but generally speaking, curly braces represent sets, and the internal elements are unordered. The authors' use of this method to represent one-to-one correspondence is inappropriate. (3) Some references have incorrect citation formats. When the number of authors exceeds 5, use "et al" for the abbreviation. The citation format for conference papers is "in Proc". Some journals do not include "vol" and "no" in their citations, such as [17] and [18]. Some journal citations do not include months.

Response:

We have carefully revised the issues as suggested by the reviewer and checked the full text. Specifically, we have changed the tense of the literature research in the Introduction to the simple past tense, we have changed the expression of beamwidth to $[X, Y, Z \dots] = [x1, y1, z1 \dots]$ in the figures and text, and we have corrected all incorrect citation formatting.

Response to Reviewer 3's Comments

Comment 3.1:

The concepts of non-reciprocal and asymmetric can be further clarified. Compared to traditional communications, what are the differences and challenges to channel modeling?

Response:

The detailed answers to the reviewer's questions are as follows, and we have also briefly described them in the paper.

For the first question, the "asymmetric" refers to the different antenna beam architecture deployed in DL and UL directions for both BS and MS sides, and the "non-reciprocal" refers to the different channel characteristics of DL and UL resulting from the former.

For the second question, the differences are explained below. For traditional MIMO communication systems, the DL and UL channel characteristics are consistent and have reciprocity, namely, only the channel on one side needs to be modeled, and the electromagnetic wave propagation trajectory of the channel on the other side is theoretically identical. However, in asymmetric massive MIMO systems, due to different beam patterns deployed for transmitting and receiving arrays, electromagnetic waves experience different propagation processes in the DL and UL channels. As a consequence, channel responses and characteristics are not identical anymore in the DL and UL and need to be modeled separately.

Moreover, the challenges to non-reciprocal channel modeling are divided into three aspects, and we effectively address them in the paper. **First, how to couple the beam domain and the scattering environment.** We establish a pyramidal beam model to select the scatterers that affect propagation and organically combine the beam domain and the propagation environment. **Second, how to establish and utilize the relationship between the DL and UL channels.** Based on the double-sphere model, we propose the concepts of scatterer reuse and effective scatterer, which not only satisfies spatial consistency but also makes full use of the relationship of DL and UL channels. We derive and analyze the correlation function of both sides. **Third, how to simultaneously model the DL and UL channels to reduce complexity.** In the case where the DL and UL channels are inconsistent, they need to be modeled separately, that is, the complexity is about twice that of the traditional communication system. In essence, it does not consider the internal correlation of the DL and UL channels but regards the two as independent systems. By modeling the correlation of both sides, the channel responses can be generated simultaneously via one simulation.

In the fourth paragraph of the Introduction on page 2, we have briefly elaborated on the above issues as follows: "Meanwhile, due to different beam patterns deployed for transmitting and receiving arrays, electromagnetic waves experience different propagation processes in the DL and UL channels, which is different from traditional symmetric communication systems. As a consequence, channel responses and characteristics are not identical anymore in the DL and UL, and non-reciprocal channels are formed resulting from asymmetric beam configurations. The challenges to non-reciprocal channel modeling lie in how to couple the beam domain and the scattering environment, how to establish and utilize the relationship between both directions, and how to simultaneously model the DL and UL channels to reduce complexity."

Comment 3.2:

What are the main novelties compared to current GBSMs? Apart from the antenna pattern and scattering generation difference, it seems to be the same with current channel models in the literature.

Response:

Apart from the antenna pattern and scattering generation difference, we also establish and utilize the correlation between DL and UL channels, embed the THz propagation properties that match real channels in the proposed model, and modify the double-sphere geometric model to support the large bandwidth, which do not appear in current GBSMs. Detailed explanations are as follows, and we have clearly shown the novelties in the revised manuscript.

(1) We fill the research gap in non-reciprocal channel modeling.

The existing GBSMs cannot be applied to the asymmetric massive MIMO systems, like in [A], [5], and [36-40], because they cannot establish and utilize the relationship between DL and UL channels. In addition, the above channel models are all based on the assumption of twin clusters. The positions and parameters of the clusters and rays are randomly generated in each simulation, and the spatial consistency after coupling with the beam domain cannot be guaranteed. Due to those problems and the excellent performance of asymmetric massive MIMO systems, channel modeling under this configuration is very meaningful but challenging work.

[A] L. Bai, Z. Huang, X. Zhang, and X. Cheng, "A non-stationary 3D model for 6G massive MIMO mmWave UAV channels," *IEEE Trans. Wireless Commun.*, vol. 21, no. 6, pp. 4325-4339, Jun. 2022.

Our research for the first time fills this research gap. We propose the beam model and the concept of effective scatterers (including the generation algorithm). By using the correlation of DL and UL channels, the model can simultaneously generate bidirectional channels, and it also has spatial consistency while reducing complexity. At the same time, we for the first time give the analytical formula and simulation results of the correlation function of the DL and UL channels. The above research results are not involved in the existing GBSMs research.

(2) We embed the THz propagation properties that match real channels in the proposed model.

In the existing work on GBSMs, no one can accurately and completely characterize the THz channel propagation characteristics in the urban scenario.

In [36], the authors modeled the THz channels in terms of clusters and assumed that the center of the cluster was a specular path. In [37], molecular absorption and diffuse scattering were considered, which were only applied to the indoor scenario. In [38], only the molecular absorption was modeled. In [39], the molecular absorption and diffuse scattering were not taken into account. In [40], the oxygen molecules absorption loss was considered, but the absorption loss of water molecules was not considered, which is also very important in the THz band.

We design the molecular absorption and diffuse scattering model for the urban THz scenario and give detailed implementation steps. By comparing with the measured data in Fig. 5, we verify that the proposed model can accurately characterize the THz

attenuation characteristics.

Moreover, the ultra-large bandwidth of the THz frequency band makes the multipath resolution extremely high, and the multipath clustering phenomenon is weak, which is proven by THz channel measurements [B, C]. Thus, the THz attenuation model we have designed acts on each ray separately, which is more suitable for the high-resolution characteristics of the THz frequency band.

[B] F. Undi, A. Schultze, W. Keusgen, M. Peter, and T. Eichler, "Angle-resolved THz channel measurements at 300 GHz in an outdoor environment," in *Proc. IEEE Inter. Conf. Commun. Workshops (ICC Wkshps)*, 2021, pp. 1-7.

[C] M. Schmieder *et al.*, "THz channel sounding: Design and validation of a high performance channel sounder at 300 GHz," in *Proc. IEEE Wireless Commun. Networking Conf. Workshops (WCNCW)*, 2020, pp. 1-6.

(3) We modify the double-sphere geometric model to support the large bandwidth.

Due to the large bandwidth of the THz frequency band, the THz channel model needs to provide high delay resolution. However, the existing double-sphere model like [39] cannot be applied to broadband channels, because the two spheres are directly connected, resulting in low delay resolution. We modify the double-sphere model by adding virtual links between the two spheres, making the model usable for THz wideband systems.

In addition, the reason for adopting the double-sphere model is this method is more suitable for THz asymmetric systems. The conventional twin-cluster stochastic model in [A], [36-38], and [40] makes it difficult to couple the beam domain, and it cannot establish and utilize the relationship between DL and UL channels and generate bidirectional channel responses at the same time. Meanwhile, the twin-cluster model is not effective for short-distance spatial consistency. The double-sphere model can just solve the above problems.

In the seventh paragraph of the Introduction on page 2, we have briefly illustrated the novelties as follows: "Compared with the existing models, there are three aspects of improvement. First, we establish and utilize the relationship between DL and UL channels and generate correlated bidirectional channel responses simultaneously, thus reducing complexity and maintaining spatial consistency. Second, the molecular absorption and diffuse scattering are considered for each ray to fit THz propagation properties. Third, we improve the double-sphere model by adding virtual links to meet the requirement of large bandwidth."

Comment 3.3:

For Fig. 6, it is better to provide the detailed parameter configurations.

Response:

We have provided the detailed parameter configurations of Fig. 6 (now Fig. 5) in the title of the figure.

Comment 3.4:

Section III: As it takes time to change the antenna configuration for UL and DL, it is not possible to show their correlation at the same time instant t_0 . Is it right?

Response:

We agree that it takes time to change the antenna configuration for UL and DL, and it is not rigorous to show their correlation at the same time instant t_0 .

In response to this problem, we have consulted the authors in [10] who built the asymmetric massive MIMO hardware system. The conclusions are as follows. The switching of UL and DL communications is done by a radio frequency electromagnetic switch instead of a manual switch, and the switching time is within $1 \mu\text{s}$, which is far shorter than the channel coherence time. Therefore, we can completely consider that the channel is static during the switching time, and there will be no deviation in the calculation of the correlation function.

To avoid misunderstandings by readers, we have added an elaboration on this issue in the paper. In Section III-A on page 7, we have explained this problem as follows: “It is noted that the computation of the correlation function is not strictly at the same time. The switching of UL and DL communications is done by a radio frequency electromagnetic switch, and the switching time is within $1 \mu\text{s}$, which is far shorter than the channel coherence time. Therefore, we consider the channel to be static during the switching time.”.

Comment 3.5:

In Section IV, more details can be given on how to set the parameters.

Response:

We have carefully checked the simulation parameters in Section IV, and all the parameters needed for the simulation have been provided. In addition, because the central frequency and beamwidth parameters are adjusted according to simulation requirements, e.g., the beamwidth needs to be adjusted in Fig. 8, and the central frequency needs to be adjusted in Fig. 10, we have given the central frequency and the beamwidth parameters separately in the titles of all figures.

Comment 3.6:

Compared to traditional communication channels, what are the difference in statistical properties of non-reciprocal channels?

Response:

We have added the comparative experiments of statistical properties of non-reciprocal channels and the traditional communication channel, and the results are shown in Table III on page 10. Compared with the traditional channel, the non-reciprocal channels have smaller path loss values and RMS delay spread values, so have better directional radiation characteristics and can maximize the use of energy, thereby improving the system efficiency.

In the third paragraph of Section IV on page 10, we have added the contents as follows: “To further illustrate the properties of non-reciprocal channels, we compare the mean values of path loss and RMS delay spread between non-reciprocal channels and the traditional omnidirectional channel. The value of D is set from 50 m to 100 m, and we take a sample point every 0.1 m. The results are shown in Table III. The values of path loss and RMS delay spread of the traditional channel are both larger than

1
2
3
4
5
6
7
8
9
10
11
12
13
14
15
16
17
18
19
20
21
22
23
24
25
26
27
28
29
30
31
32
33
34
35
36
37
38
39
40
41
42
43
44
45
46
47
48
49
50
51
52
53
54
55
56
57
58
59
60

the non-reciprocal channels. It can be seen that the non-reciprocal channels have better directional radiation characteristics and can maximize the use of energy, thereby improving the system efficiency.”.